INORGANIC CHEMISTRY FRONTIERS

REVIEW

View Article Online
View Journal | View Issue

Cite this: *Inorg. Chem. Front.*, 2025, **12**, 4741

Innovations in scintillator materials for X-ray detection

Kuilin Li,† Wenqing Li,† Qi Nie* and Xiao Luo *

Since their introduction in the early 20th century, scintillators have become essential components of a wide range of applications, including high-energy physics, medical imaging, cryptography, and nuclear detection. As the demand for high-performance scintillating materials continues to rise in particle physics experiments and medical imaging technologies, the development of novel scintillator materials has become a critical area of research. In recent years, advancements in scintillators have flourished, presenting new opportunities for practical applications. This review presents a comprehensive overview of standard performance parameters for scintillators, aimed at enhancing our understanding and evaluating their advancements. Unlike previous reviews focusing on isolated material categories, this work provides a cross-comparative analysis of emerging scintillators, with particular emphasis on challenges for high-precision detection and low-dose imaging. We highlight the latest developments in scintillator materials, emphasizing research from the past three years and focusing on their intrinsic properties. Our analysis covers the perovskite scintillators, nanocluster scintillators, rare-earth ion-doped scintillators, organic scintillators, and scintillators with specialized structures. This classification offers a scientific perspective on the overall progress in the field of scintillators, and several forward-looking insights into the future development of scintillators are proposed, employing a problem-oriented approach. Future scintillator development requires synergistic material design integrating computational modeling and scalable fabrication techniques to enhance stability, radiation tolerance, and light yields. Prioritizing lead-free systems and defect-tolerant lattice engineering will address environmental and operational challenges, and advancements in hybrid architectures, and novel optical structures promise breakthroughs in low-dose imaging, industrial nondestructive testing and sustainable radiation detection technologies. Eventually, we discuss the challenges encountered in scintillator development, explore future prospects, and provide valuable insights for improving their performances and expanding their applications.

Received 7th March 2025,
Accepted 7th April 2025

DOI: 10.1039/d5qi00671f

rsc.li/frontiers-inorganic

1. Introduction

X-rays are a form of electromagnetic radiation with exceedingly short wavelengths, typically ranging from 0.01 to 10 nm. Their remarkable penetrating power and high energy enable them to traverse various materials, including soft tissues in the human body and denser substances. Due to their exceptional capacity for penetration and imaging, X-rays find extensive application across multiple domains, such as medical imaging, industrial non-destructive testing, encryption and security screenings.[1–5] Since the groundbreaking discovery of X-rays by Wilhelm Röntgen in 1895,[6] this technology has rapidly evolved and made significant strides, gradually becoming an indispensable part of modern science and technology. Röntgen's discovery not only spurred in-depth investigations into the properties and behavior of X-rays but also ushered in a new era in imaging science, providing a novel tool for medical diagnosis.[7] Through modalities such as X-ray films, computed tomography (CT), and digital imaging, physicians can observe the internal structures and lesions of patients with remarkable clarity, vastly improving the quality and efficacy of medical services. Consequently, the development of materials capable of detecting X-rays at low radiation doses is crucial.[8] Furthermore, this technology adeptly identifies welding defects, internal cracks, and other structural issues, ensuring product quality and operational safety.

X-ray detection can be categorized into direct and indirect methods based on different detection principles (Fig. 1). Direct detection involves the direct absorption of X-rays, which are then converted into electronic or biochemical signals.[9] In contrast, indirect detection involves the conversion of X-rays into visible light or ultraviolet light using scintillation materials, followed by detection with optical devices such as

School of Optoelectronic Science and Engineering, University of Electronic Science and Technology of China (UESTC), Chengdu 610054, PR China.
E-mail: uestcnq@outlook.com, luox@uestc.edu.cn
† These authors contributed equally to this work.

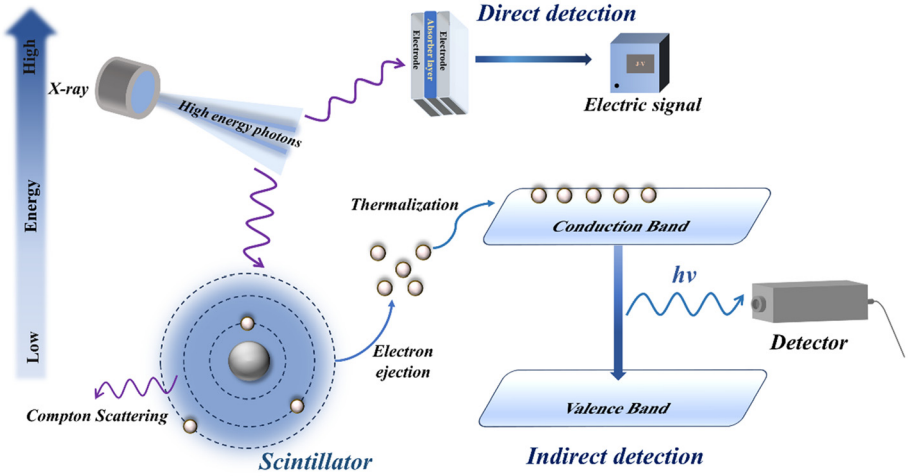

Fig. 1 Schematic diagram of the principles of direct and indirect X-ray detection.

photomultiplier tubes, charge-coupled devices, or complementary metal–oxide–semiconductor detectors.[10] Indirect detection is generally more cost-effective than direct detection, and the availability of various scintillators allows for diverse applications, making them increasingly popular. Practically, take biological X-ray imaging as an example, X-rays pass through the biological specimen and create an image on the scintillator film. Then the scintillator film converts the high-energy X-ray image into a signal that can be detected by conventional imaging devices. Subsequently, this signal is processed by the corresponding software and transformed into an image that is recognizable by the human eye. Therefore, high-quality scintillator films are crucial in the application process.

Scintillators are indispensable components of indirect detection. When high-energy particles or electromagnetic radiation traverse the scintillators, they interact with the atoms within the material, exciting them to excited states. As these atoms return to their ground states, they release energy in the form of photons, emitting visible light or radiation of other wavelengths. After a long period of development, numerous traditional scintillators, characterized by their high light yield (LY) and exceptional energy resolution, have achieved commercial viability for their respective applications. For instance, due to their exceptionally high LYs, NaI:Tl and CsI:Tl have been utilized in medical imaging, X-ray detection, and medical radiography.[11–13] $Bi_4Ge_3O_{12}$ (BGO) is widely accepted as an commercial-applicable inorganic scintillator due to its mechanically stable oxide with proportional performance.[14,15] Moreover, single-crystalline $Lu_{1.8}Y_{0.2}SiO_5$:Ce is employed in positron emission tomography (PET), while $GdWO_4$ and Gd_2O_2S:Tb are used in CT.[16–18] Additionally, $Y_3Al_5O_{12}$:Ce and BaF_2 are utilized in high energy physics experiments.[19,20] Despite their widespread application, these traditional scintillators still suffer from some drawbacks. The preparation of traditional scintillator materials typically entails a complex process, high temperatures, and the use of capital-intensive equipment, resulting in considerable costs.[16,21,22] Furthermore, due to their intrinsic characteristics, these materials inevitably experience interference from a long afterglow, light scattering, and relatively low detection limit.[23] Additionally, their inflexible nature and biotoxicity limit their potential for advancement. Moreover, the challenges in converting the radiation emission wavelength into the visible light spectrum further hinder their applicability.[24]

Recently, the rapid advancement of scintillator materials, driven by extensive and in-depth research, has captivated more researchers each year. Among these, metal halides have garnered significant attention due to their intriguing luminescence properties and high LYs. Since Chen *et al.* utilized fully inorganic perovskite nanocrystals as scintillators in 2018,[24] achieving strong X-ray absorption, intense radioluminescence (RL) at visible wavelengths, flexibility, and ultra-low detection limits, the development of metal halides has progressed by leaps and bounds. Accordingly, many studies have comprehensively summarized recent research advancements in scintillator materials. For instance, in 2023, Wang *et al.* summarized strategies for enhancing the LY of halide perovskite scintillators and presented a roadmap for improving X-ray imaging performance.[25] Zhou *et al.* summarized the latest advancements in low-dimensional metal halide scintillators and proposed future development directions.[26] Some studies have predominantly concentrated on specific categories of scintillator materials. Fan *et al.* focused on reviewing the progress of organic–inorganic hybrid Mn(II) halide scintillators[27] and Zhao *et al.* summarized advanced techniques for preparing rare-earth nanocrystalline scintillators and provided essential guidance for their application in biomedical research.[28] Besides, rare-earth-doped nano-scintillators have emerged as prominent scintillators in the field of biomedical applications. For example, Hong *et al.* presented a summary of the latest developments in advanced X-ray luminescence, focusing on its applications in imaging, biosensing, theragnostics, and neuromodulation through optogenetics.[8] In 2024, Md. Helal Miah *et al.* summarized advancements in X-ray detection technologies across various materials, with a focus on meth-

odologies, structural designs, and device architectures. Notably, the review provides crucial insights into advances in perovskite materials for X-ray detection and imaging applications, emphasizing strategies to optimize efficiency, stability, and scalability for next-generation radiation sensing systems. To conclude, the development of scintillators is both extensive and profound. However, there is a noticeable absence of a comprehensive return to the development of advanced scintillator materials.

In this review, we initially summarize a set of standard performance parameters for scintillators to facilitate a deeper understanding and evaluation of their development. We update the latest developments in scintillator materials based on their inherent properties, with a particular focus on research from the past three years. Then we focus on scintillators containing lead and lead-free scintillators, Cu-based clusters, rare-earth-ion-doped scintillators, organic scintillators as well as certain specialized structures. Our classification provides a scientific overview of the overall development of scintillators, aiding researchers in gaining a comprehensive understanding of the latest advancements in the field. Ultimately, this review also addresses the challenges faced in the development of scintillators, analyzes the prospects for their future advancement, and offers insightful visions for enhancing the performance of scintillators and their applications. Unlike prior reviews that adopt siloed discussions of conventional material systems, this study pioneers a systematic cross-disciplinary assessment of next-generation scintillators, encompassing metal halide perovskites, copper-based nanoclusters, rare-earth nanocrystallites and triplet-harvesting organic matrices. By critically evaluating their interdependent photophysical limitations, such as ion migration in perovskites, environmental instability in Cu-based architectures, and triplet exciton quenching in organic systems, we have a clear and comprehensive understanding of the advantages and disadvantages of each material in the new generation of scintillators.

2. Principle

In this section, we focus on the intricate details of both material and device characteristics, with particular emphasis on the interdependence between them. The performance and features of the device are inevitably shaped by inherent properties of the materials employed. This comprehensive exploration aims to elucidate the complex relationship between material characteristics and the corresponding performance metrics of the device, thereby providing the reader with a deeper understanding of the subsequent content.

2.1 Light yield and overall conversion efficiency for X-rays

The LY represents the ability of a scintillator to convert high-energy rays into low-energy visible light, which can be expressed as follows:

$$\mathrm{LY} = 1\,000\,000\frac{SQ}{\beta E_g} \quad (1)$$

where S represents the transmission efficiency of electron–hole pairs to the optical emission centers, Q denotes the photoluminescence (PL) efficiency, β is a constant typically valued at 2.5, and E_g is the energy band gap. In scintillators, the standard time gate is usually set between 100 ns and 10 μs, and the exact value is determined through practical experimentation. A high-energy LY is essential for scintillators. Moreover, the overall conversion efficiency of X-rays in the scintillator can be defined as the number of UV/visible photons (N_{ph}) generated during the scintillation conversion process per unit energy (E) of an incoming X-ray photon:

$$N_{ph} = \frac{E/\beta E_g}{SQ} \quad (2)$$

2.2 Attenuation coefficient

The attenuation coefficient (AC) indicates how effectively the detection material can absorb high-energy rays. It has a positive correlation with both its density ρ and effective atomic number Z_{eff}. The attenuation coefficient is directly proportional to these factors and can be expressed as:

$$\mathrm{AC} = \frac{\rho {Z_{eff}}^4}{AE^2} \quad (3)$$

where A is the atomic mass and E is the radiation energy. This equation indicates that heavy elements and a high crystal density prevail in scintillators.

2.3 Afterglow

Afterglow refers to the time required for the intensity of RL in scintillators to diminish to a certain level after X-ray exposure. Due to the superimposition of previously exposed signals, prolonged afterglow can result in imaging artifacts. Therefore, a shorter afterglow duration is more desirable for common occasions. Yet along with the extension of scintillator applications, a long afterglow can be welcomed in some particular situations, like imaging scenes with memory properties, which are discussed in the following sections.

2.4 Spatial resolution

Spatial resolution pertains to the capacity to discern adjacent details within an object and their relative clarity. Specifically, higher spatial resolution is indicative of superior image quality. In scintillators, spatial resolution is primarily influenced by the geometric shape and intrinsic morphology of the scintillator itself, including its shape, size, and thickness. It has been widely accepted that the modulation transfer function (MTF), equivalent to 0.2, is derived from X-ray imaging to characterize spatial resolution. This also reflects the limitations of human visual discernment, typically measured in line pairs per millimeter (lp mm^{-1}). It is important to note that the thickness of the scintillator significantly impacts imaging resolution. Thus, for discussions concerning scintillators in studies, it is essential to address both spatial resolution and thickness concurrently.

2.5 Linear response of scintillators and matching with RL and the photodetector's spectrum

RL refers to visible or near-visible light emitted by a scintillator under the excitation of ionizing radiation. For the RL of scintillators, the radiation intensity must have a linear relationship with the dose of X-rays. Moreover, the wavelength of the RL needs to match the efficient operational wavelength region of the detector. It is also very important to select an appropriate detector for different scintillators.

2.6 Detection limit

The detection limit is defined as the equivalent dose rate that generates a signal three times that of the noise level. The captured signal should be recognized as valid only when the incident X-ray dose exceeds this limit. To lower this threshold and enhance sensitivity, it is crucial to minimize the dark current and improve the signal-to-noise ratio. In medical imaging, a smaller detection limit reduces the exposure to X-rays and thereby minimizes the potential harm to biological tissues.

2.7 Chemical stability and radiation resistance

Chemical stability is a crucial indicator of a scintillator's ability to maintain its performance under various environmental conditions, including moisture resistance, temperature fluctuations, and oxidation resistance. For instance, CsI and NaI:Tl may undergo degradation in high-humidity environments, resulting in decreased luminescence efficiency. As for the radiation resistance, it is a key factor when assessing the ability of scintillator materials to preserve their performance upon exposure to high-energy radiation. Under exposure to high doses of X-rays, the lattice structure of scintillator materials may sustain damage, leading to a reduction in light output and a decline in energy resolution. Enhancing both chemical stability and radiation resistance can significantly improve the performance of X-ray scintillators. This enables them to maintain excellent detection capabilities and application efficacy in various harsh environments.

3. Technology innovations

This section provides a categorized overview of commonly used scintillator materials, highlighting their types, characteristics, recent representative works, and potential issues (Fig. 2). First, we introduce lead-based perovskite scintillators, which have been the subject of extensive research due to the strong X-ray absorption properties of Pb. This category

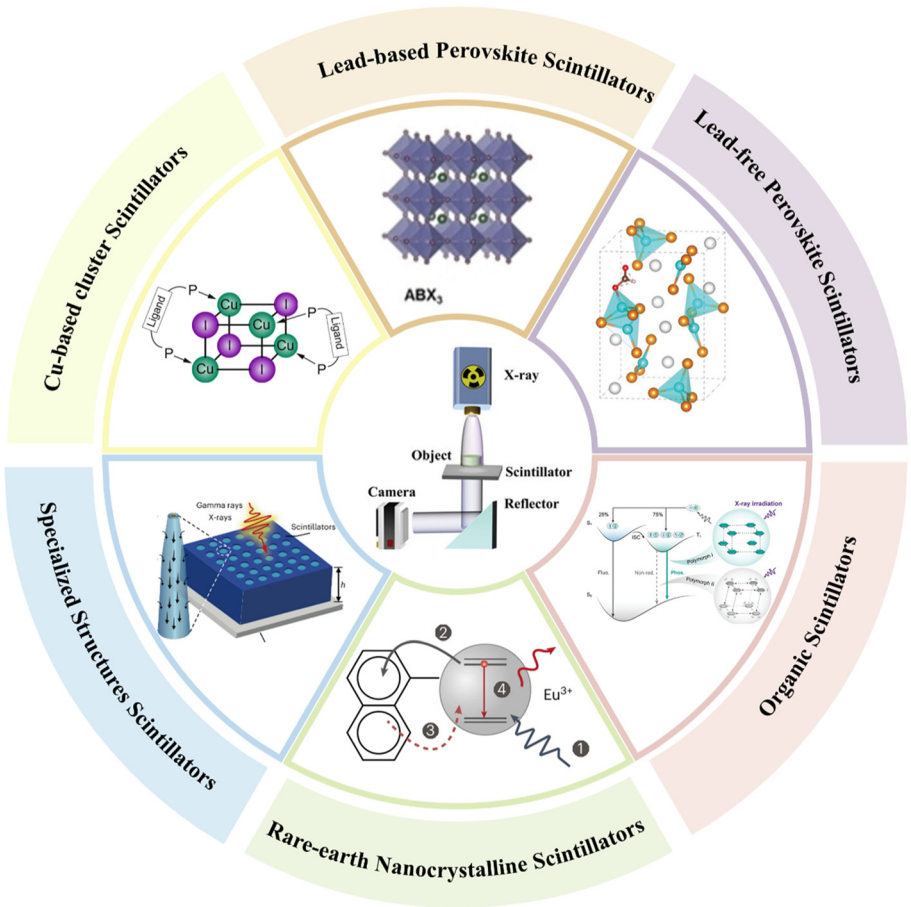

Fig. 2 Brief overview of this review.

remains active, with new studies continuously emerging. Next, we focus on lead-free scintillators, which have gained significant attention in recent years due to environmental and sustainable development concerns. Among these, copper-based scintillators are considered an excellent alternative to Pb and represent the main category within lead-free materials, as discussed in section 3.2.2. Additionally, there has been increasing interest in emerging copper-based nanoclusters, which are also being explored as scintillator materials, due to their exceptional optical properties. Rare earth elements, commonly used in optical materials, have attracted significant attention for their ability to regulate energy levels, with numerous applications in X-ray scintillators, which we address in detail in section 3.4. Furthermore, organic materials, due to their controllability and structural diversity, have also been extensively researched within the field of scintillators. Lastly, we present an overview of special structures in the scintillator domain, incorporating recent advancements and relevant studies.

3.1 Lead-based perovskite scintillators

Benefiting from adjustable bandgaps, high spatial resolution, fast response times, high LYs and considerable X-ray attenuation,[24,29–32] lead-based perovskite scintillators have consistently been a major focus of research efforts and many valuable efforts have explored these charming materials (Table 1).[24,33–52] Nevertheless, they still suffer from several drawbacks. The instability of a perovskite is always a non-negligible issue because of its hygroscopicity. Water and oxygen expand perovskite molecules, causing aggregation and affecting their optical properties, which will even be prominent under irradiation with X-rays,[53] and the typical method for improving a perovskite's stability is to passivate its surface or reduce inner defects. Favorable and accepted methods are to embed them in solid substances or encapsulate them with polymers like polyethylene glycol terephthalate (PET), polytetrafluoroethylene (PTFE) and poly(methyl methacrylate) (PMMA).[54]

Based on similar methodologies, some groups have already completed related work,[55,56] and in the past two years more noteworthy studies have been reported. Lv *et al.* combined $CsPbBr_3$ nanocrystals with PMMA to fabricate a perovskite film of over 100 cm^2 with a root-mean-square roughness of 1.06 nm, which retained 96% initial luminous intensity in water and an ambient environment for 480 h and 2880 h (Fig. 3a).[57] Zheng *et al.* selected poly(maleic anhydride-*alt*-1-octadecene) (PMAO) with a low molecular weight (M_n = 1911) as the multi-dentate ligands and synthesized PMAO–$CsPbBr_3$ lead perovskite nanocrystals (PNCs) *via* hot injection. It shows preeminent water stability, maintaining its fluorescence for 2600 min while traditional PNCs became completely dysfunctional after 100 min, as observed in Fig. 3b.[58] For the embedded-in-matrix strategy, Shen *et al.* applied cold-sintered technology to bulk scintillators to fabricate $CsPbBr_3$ nanocrystals embedded in the Cs_4PbBr_6 structure based on an "emitter-in-matrix" principle (Fig. 3c).[59] This group employed a rather low temperature of 90 °C during the sintering process and DMSO was introduced as the antisolvent to promote its densification (Fig. 3d). Compared to solid-state sintering at high temperature, cold sintering demonstrates highly compacted grains with enhanced densification and transparency, thus scattering can be well controlled. These bulk scintillators exhibit a high LY of 33 800 photons per MeV, a low detection limit of 79 $nGy_{air}\ s^{-1}$ and outstanding spatial resolution of 8.9 lp mm^{-1}.

Apart from those tactics mentioned for enhancing perovskite stability, some other interesting methods have appeared. Chen *et al.* found it detrimental to cross-linking of the organosilicon matrix that the silicon-based $CsPbBr_3$ encapsulated nanocrystals were linked with long-carbon-chain ligands, thus suffering from poor transparency and surface roughness.[60] Yet this can be improved by substituting long chain ligands for short ones (Fig. 3e). Then a dual-organosilicon ligand system was proposed, consisting of (3-aminopropyl)triethoxysilane (APTES) and (3-aminopropyl)-triethoxysilane with pentanedioic anhydride (APTES-PA), and the scintillator showed a satisfying spatial resolution above 20 lp mm^{-1} and high stability in various harsh environments. Wu *et al.* applied the host–guest strategy, involving confining $MAPbBr_3$ nanocrystals in metal–organic frameworks (MOFs) (Fig. 3f).[61] The *in situ* spatial confinement provides quantum confinement and surface passivation, resulting in significant stability against air, heat and irradiation. It exhibits a detection limit of 170 $nGy_{air}\ s^{-1}$ and an impressive spatial resolution of 14.7 lp mm^{-1}. Likewise, Li *et al.* presented a glass-ceramic $CsPbBr_3$ perovskite film with high transparency, in which $CsPbBr_3$ crystals grew *in situ*.[62] The thickness was controlled by the crystal coordination–topology growth and *in situ* film formation strategy, resulting in little light scattering and a uniform distribution of the perovs-

Table 1 The parameters of lead-based scintillators

Material	Type	Light yield (photons per MeV)	Detection limit ($nGy_{air}\ s^{-1}$)	Spatial resolution (lp mm^{-1})	Ref.
$CsPbBr_3$	Nanocrystals	9001	—	9	57
$CsPbBr_3$	Nanocrystals	—	—	—	58
$CsPbBr_3/Cs_4PbBr_6$	Nanocrystals	33 800	79	8.9	59
$CsPbBr_3$	Nanocrystals	—	—	20	60
$MAPbBr_3$	MOFs	—	170	14.7	61
$CsPbBr_3$	Nanocrystals	—	326	13.9	62
$MAPbMgZnCdBr_3$	Nanocrystals	21 200	462	11.7	63
$CsPb_2Br_5:K^+$	Nanocrystals	25 160	162.3	21	64

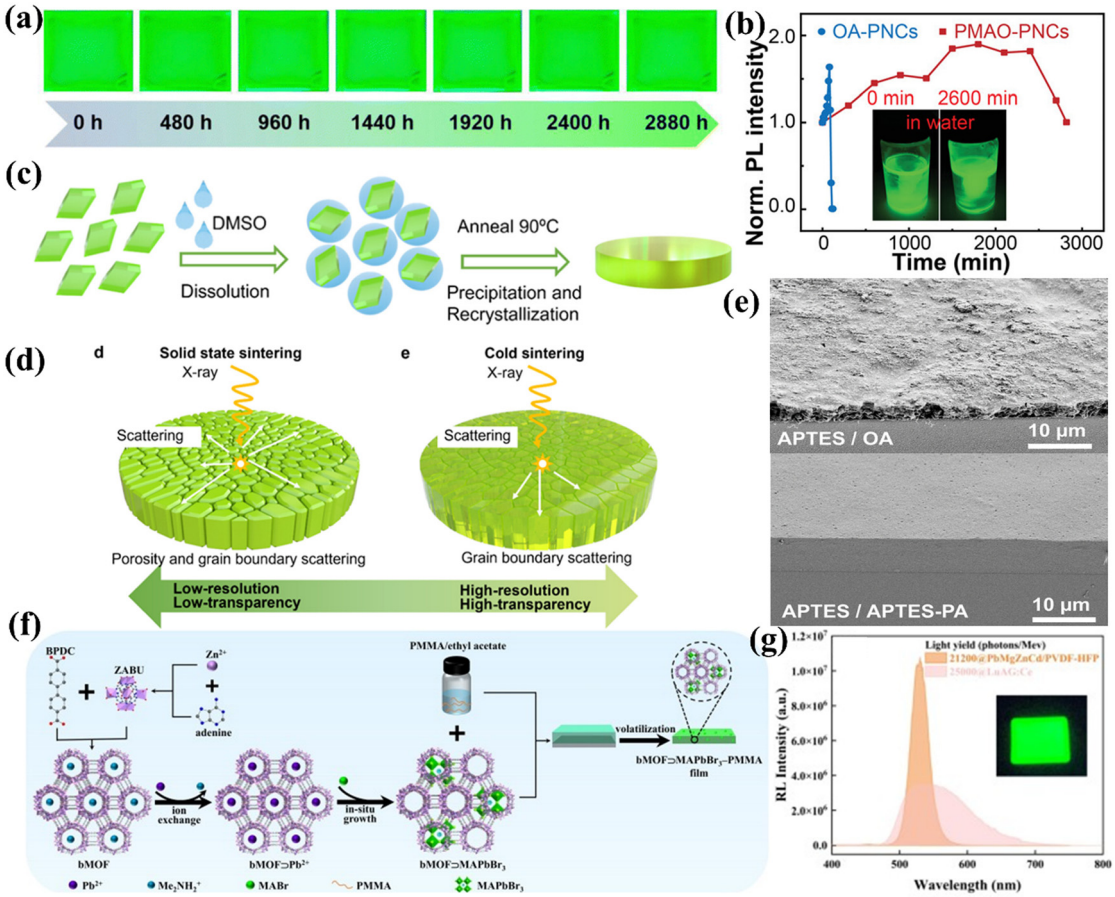

Fig. 3 (a) Photographs of the $CsPbBr_3$@PMMA@VmB1 film in air at various times to show its stability. (b) PL evolution of PNCs after being immersed in water for different times (inset: optical images of the PMAO-PNCs in water under vigorous stirring). (c) Design of the fabrication process to obtain bulk $CsPbBr_3/Cs_4PbBr_6$ ceramic composite pellets *via* a CSP. (d) Light scattering of residual pores and grain boundaries in conventional solid-state sintered ceramics, reducing energy resolution and transparency (left). Reduction of light scattering from grain boundaries in cold-sintered ceramics to enhance resolution and transparency (right). (e) SEM images of the PNC/silicone films with APTES/OA ligands (upper) and APTES/APTES-PA ligands (bottom). (f) Schematic illustration of the synthesis of bMOF–$MAPbBr_3$ and bMOF–$MAPbBr_3$–PMMA films. (g) Comparison of LY between the $MAPbMgZnCdBr_3$/PVDF-HFP scintillator and LuAG:Ce.

kite crystals. The as synthesized 250 μm film enables a detection limit of 326 nGy_{air} s^{-1} and a high spatial resolution of 13.9 lp mm^{-1} with incredible stability under exposure to long-term X-ray irradiation, water soaking and high temperature.

Besides the stability improvements, progress was also made in the energy utilization efficiency by doping with new elements. Xiang *et al.* performed calculations on the surface formation energy and the vacancy defect energy and co-doped several bivalent metal ions to substitute Pb in $MAPbBr_3$ to improve the photoluminescence quantum yield (PLQY) and decay time of the nanocrystal.[63] Furthermore, the scintillator was fabricated using $MAPbMgZnCdBr_3$ as the energy conversion layer with PVDF-HFP as the carrier and demonstrated a LY of 21 200 photons per MeV (Fig. 3g) with a spatial resolution of 11.7 lp mm^{-1}. Moreover, Qiu *et al.* doped non-emissive $CsPb_2Br_5$ with alkali metals, which caused lattice distortion and enhanced electron–phonon coupling.[64] This led to the formation of potential transient energy wells, resulting in the creation of self-trapped excitons (STEs) generated by X-rays. The STE experiences radiative recombination, with a PLQY of 55.92%, thus X-rays can be transformed into red light. Furthermore, the K^+-doped $CsPb_2Br_5$ based X-ray scintillator displays high stability and weak self-absorption with a detection limit of 162.3 nGy_{air} s^{-1} and 21 lp mm^{-1}.

Despite being a long-investigated scintillator material, it still suffers from non-negligible drawbacks. The predominant emission mechanism *via* band-edge excitons introduces substantial self-absorption effects owing to spectral overlap between its emission and absorption profiles. This fundamental limitation persists as a pervasive challenge inherent to virtually all perovskite-based systems. While lead-based perovskite scintillators exhibit unparalleled performance metrics, the absence of innovative stabilization strategies remains a critical bottleneck. No groundbreaking processing techniques addressing environmental robustness have emerged in the latest literature, which confines their practical deployment to laboratory-scale demonstrations or strictly controlled environments, as evidenced by rapid performance degradation. In addition,

the potential environmental leakage risk of heavy metals further hinders large-scale applications.

3.2 Lead-free perovskite scintillators

Although Pb based scintillators exhibit promising absorption of X-rays, the heavy atom's intrinsic toxicity, doing harm to human health and environment, is still a non-negligible hindrance to its extensive applications. Therefore, the pursuit of 'lead-free' scintillators has been put forward, expecting materials with no toxic element yet retaining exceptional and controllable properties. In recent years, research on lead-free scintillators has significantly outpaced that on traditional lead-based scintillators, especially in the past two years (Table 2).[65–67] These materials can be categorized into the following types: double perovskite scintillators, manganese-based halide scintillators and others; these are all introduced and discussed in the following sections.

3.2.1 Copper-free scintillators. One of the important forms of copper-free scintillator materials is the double perovskite material. Their development stemmed from the recognition that, while perovskite materials have long been a focus of scintillator research due to the advantages in their synthesis, the isolated network of metal-halide octahedral units leads to poor carrier mobility and predominantly indirect bandgap characteristics.[68–70] In contrast, the double perovskite materials, typically represented as $A_2B_3X_6$ (where A is a monovalent metal ion like Ag^+ and Cs^+, B is a trivalent metal ion like In^{3+} and Sb^{3+}, X refers to a halide anion), though suffering from lower carrier mobility and a larger indirect bandgap compared to the perovskites, possess a cubic structure with interlinked $[B^+X_6]^{5-}$ and $[B^+X_6]^{3-}$ sites and do not contain toxic Pb elements.[69,71–73] This objectively enhances the material's stability and environmental friendliness, making it an attractive alternative to perovskite materials for researchers. Efforts have been made to circumvent these drawbacks. For example, Varnakavi *et al.* managed to inject 4.04% of Mn(II) into a double perovskite $Cs_2NaBiCl_6$ nanocrystal (Fig. 4a), which turned out to have a PLQY of 10.6% at 586 nm, circumventing self-absorption.[74] The $Cs_2NaBiCl_6$:4.04%Mn@poly(methyl methacrylate) scintillator film demonstrates a satisfying LY of 28 350 photons per MeV and a detection limit of 45.2 nGy_{air} s^{-1}, along with a rather exceptional spatial resolution of 14.76 lp mm^{-1}. Recent advances in Bi^{3+}-doped perovskite scintillators[75] highlight their critical role in performance enhancement. In 2025, Chen *et al.* engineered 3D bismuth chloride perovskites *via* monovalent Na^+ incorporation, achieving a sensitivity of 354.5 $mCGy^{-1}$ cm^{-2} and an ultralow detection limit of 59.4 nGy s^{-1} with stable cycling over 4500 on–off cycles.[76]

Table 2 The parameters of lead-free scintillators

Material	Type	Light yield (photons per MeV)	Detection limit (nGy_{air} s^{-1})	Spatial resolution (lp mm^{-1})	Ref.
$Cs_3Cu_2I_5$:Mn	Single-crystal	95 772	—	—	100
Rb_2AgI_3:Cu^+	Single-crystal	53 983	231	14.1	101
$Cs_3Cu_2I_5$:$HCOO^-$	Single crystals	61 500	—	10	102
$Cs_3Cu_2I_5$	0D	—	12 760 000	10	103
$Cs_3Cu_2I_5$	Nanocrystals	—	105	14.3	104
$Cs_3Cu_2I_5$	Nanocrystals	—	—	—	105
$Cs_3Cu_2Cl_5$	Single crystal	95 000	2700	105	106
$CsCu_2I_3$	Crystal	—	88.9	15.6	107
$Cs_5Cu_3Cl_6I_2$	1D	64 800–67 200	—	27	108
$Cs_5Cu_3Cl_6I_2$	1D	—	—	—	109
$Cs_5Cu_3Cl_6I_2$:Rb	Crystal	64 868	—	14	110
Rb_2AgBr_3:Cu^+	Single crystal	79 250	714.83	5.8	111
Rb_2AgI_3:Cu^+	1D single crystals	36 293	1022	10.2	112
Rb_2AgBr_3:Cu^+	Single-crystal	—	—	10.2	113
$Cs_2NaBiCl_6$	Nanocrystals	28 350	45.2	14.76	74
Cs_2TeCl_6	Microcrystals	38 523	258	15.9	66
Cs_2HfCl_6	Microcrystals	21 700	55	11.2	67
$Cs_4Cd_{1-x}Mn_xBi_2Cl_{12}$	2D	34 450	183.6	16.7	77
$(C_{25}H_{22}P)_2MnCl_4$	Single crystals	78 937	—	25.61	82
$(C_{38}H_{34}P_2)MnBr_4$	Crystal	35 945	5500	16.7	83
BPP_2MnBr_4	0D	35 000	250	20	84
$(MTP)_2MnBr_4$	Crystal	67 000	82.4	6.2	85
$PrPP_2MnBr_4$	Single crystal	43 511	13.9	53.5	86
$(Br\text{-}PrTPP)_2MnBr_4$	0D	68 000	45	12.78	87
$(BTPP)_2MnX_4$	0D	53 000	89.9	14.1	88
A_2MnBr_4	0D	80 100	30	14.06	89
DMA_4InCl_7:Sb^{3+}	0D	23 500	175	—	90
$TTA_2In_{0.92}Sb_{0.08}Cl_5$	0D	60 976	90	—	91
$TpyBiCl_5$	Single crystal	—	196.31	—	92
$Ag_6S_6L_6$ (SC-Ag)	Metal cluster	17 420	—	16	93
$Ag_2Cl_2(dppb)_2$	Single crystal	79 970	59.8	25	94
$Cs_2Ag_{.6}Na_{.4}In_{.85}Bi_{.15}Cl_6$	Nanocrystals	—	—	—	95
Cs_2CdCl_4:10%Mn	Single crystal	88 138	31.04	16.1	96
Tb^{3+}–$Cs_2NaGdCl_6$	Single crystals	39 100	41.32	10.75	78
Te^{4+} dopingCs_2SnCl_6	Nanocrystals	—	132	20	79

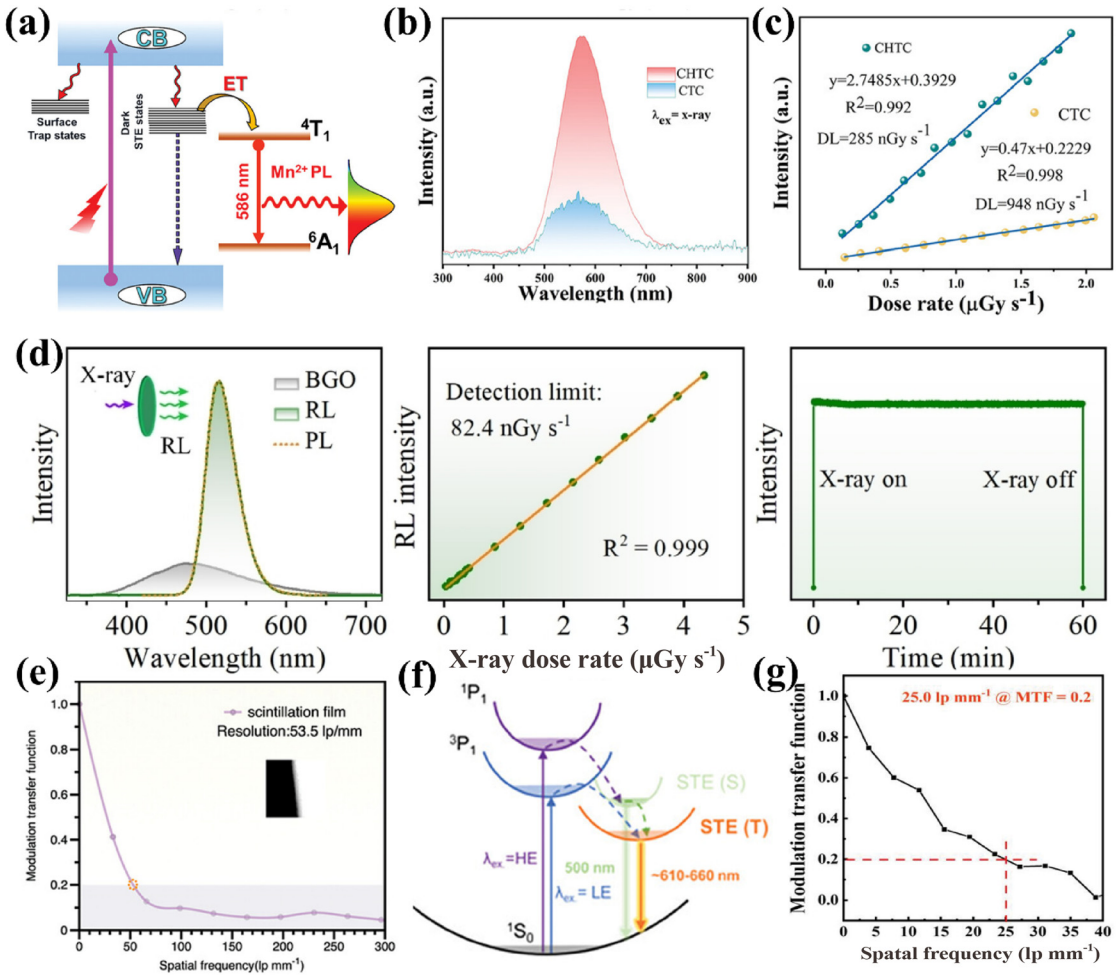

Fig. 4 (a) Schematic diagram of Mn^{2+}-doped $Cs_2NaBiCl_6$ showing STE dynamics and the Mn^{2+} PL mechanism. (b) RL of CHTC and CTC. (c) RL of CHTC and CTC as a function of dose rate. (d) RL spectra of $(MTP)_2MnBr_4$ and BGO under X-ray irradiation (left). Integrated RL intensity of $(MTP)_2MnBr_4$ as a function of X-ray dose rate (middle). Time-dependent RL intensity of $(MTP)_2MnBr_4$ upon continuous X-ray irradiation at a dose rate of 42.29 mGy s^{-1} for 60 min (right). (e) The MTF of the $PrPP_2MnBr_4$ scintillation film beveled edge image. (f) Schematic diagram of the emission mechanism with STE (T) and STE (S). (g) The MTF of the $Ag_2Cl_2(dppb)_2$ (Ag1) scintillator edge images.

Complementing this, Subagyo *et al.* demonstrated the efficacy of Bi^{3+} in optimizing radiation hardness, LY, and defect dynamics, underscoring its potential for sustainable high-performance X-ray detectors. Together, these studies exemplify the versatility of Bi^{3+} in advancing perovskite scintillators for precision radiation sensing.[65] In parallel, Lai *et al.* discovered that the Te-based double perovskite, Cs_2TeCl_6 (CTC) microcrystal, showed a broadband yellow emission which was highly matched with CCD.[66] Furthermore, the hafnium alloyed CTC scintillator, with PDMS as the binder, demonstrates a LY of 38 523 photons per MeV (Fig. 4b), a detection limit of 258 nGy_{air} s^{-1} (Fig. 4c) and an outstanding spatial resolution of 15.9 lp mm^{-1}. Likewise, Zhang *et al.* came up with Cs_2HfCl_6, and under ambient conditions for 60 days, there were no extra diffraction peaks observed in XRD spectra, indicating promising stability, which was possibly due to short Hf–Cl bonds, with a spatial resolution of 11.2 lp mm^{-1}.[67] Moreover, Li *et al.* reported a 2D layered double perovskite, namely $Cs_4Cd_{1-x}Mn_xBi_2Cl_{12}$, which demonstrated preeminent scintillation properties, including exceptional emission response linearity and a high LY of ~34 450 photons per MeV.[77] More admirably, the X-ray excited emission intensity remained at 92% and 94% respectively after being stored under an ambient atmosphere and exposed to a total dose of 11.4 Gy irradiation. After being mixed with PDMS, the scintillator screen exhibits an excellent spatial resolution of 16.7 lp mm^{-1}. Subsequently, Naresh *et al.* proposed the $Cs_2NaGdCl_6$:5%Tb^{3+} films with 0.4 mm thickness and achieved a low detection limit of 41.32 nGy_{air} s^{-1}, an LY of 39 100 photons per MeV and excellent radiation stability.[78] After the introduction of Tb^{3+}, the PLQY increased from 8.4% to 72.6% due to efficient energy transfer from STE to Tb^{3+}. Likewise, Wang *et al.* introduced Te^{4+} into the double perovskite Cs_2SnCl_6 and fabricated flexible imaging screens with a resolution of 20 lp mm^{-1} and a low detection limit of 132 nGy_{air} s^{-1}.[79]

Manganese-based halides have only been utilized in the past five years. Due to their excellent LY and high energy radi-

ation absorption performance, they are designed to be potential candidates for efficient and environmentally friendly scintillator materials.[80,81] Here we focus mainly on research published in the past year. For instance, Zhou *et al.* designed and synthesized the thickness-tunable inch-sized Mn-based halide single crystal, $(C_{25}H_{22}P)_2MnCl_4$, with a PLQY up to 99.10% and the scintillator film showed a LY of 78 937 photons per MeV and a spatial resolution of 25.61 lp mm^{-1}.[82] Liu *et al.* synthesized the $(C_{38}H_{34}P_2)MnBr_4$ organogel scintillator and made it water-stable, stretchable and self-healing by carefully arranging and activating dynamic hydrogen bonds and coordination bonds.[83] The organogel scintillator is able to be stretched up to 13-fold while maintaining its property, and the imaging resolution reached 16.7 lp mm^{-1}. The scintillator film demonstrated seamless self-healing within 30 min, providing a robust solution for the self-repair of flexible films that may experience bending or cutting damage during usage. Wang *et al.* reported a method to control the crystallization process of manganese halides through organic cation modulation.[84] This approach aims to reduce uncontrolled crystallization during the fabrication of large-area flat-panel detectors, thereby enhancing their light-emitting properties. The large steric hindrance brought by the cation provides a high exciton binding energy and restrains non-radiative recombination. The as synthesized BPP_2MnBr_4 (BPP = $C_{25}H_{22}P^+$) exhibits a superior spatial resolution of more than 20 lp mm^{-1}, an exceptional LY of over 35 000 photons per MeV and an ultra-low detection limit of less than 250 nGy_{air} s^{-1}. Likewise, Zhang *et al.* reported the potential of applying $(MTP)_2MnBr_4$ (MTP refers to methyltriphenylphosphonium) as an X-ray scintillator for its near-unity PLQY, high resistance to thermal quenching and decent stability.[85] They fabricated a thin film scintillator and determined its impressive LY of 67 000 photons per MeV and superior detection limit of 82.4 nGy s^{-1} (Fig. 4d).

Moreover, Xiao *et al.* synthesized $PrPP_2MnBr_4$ ($PrPP_2$ refers to diisopropylammonium) by a dual-solvent evaporation method, and the 10 cm × 10 cm area scintillation screen based on the solidified melt salt exhibited a LY of 43 511 photons per MeV, an unprecedented high spatial resolution of 53.5 lp mm^{-1} (Fig. 4e) and an outstanding detection limit of 13.9 nGy_{air} s^{-1}.[86] Also, Zhang *et al.*, recognizing the satisfying optical and scintillator properties of 0D organic–inorganic hybrid metal halides (OIMHs), synthesized $(Br\text{-}PrTPP)_2MnBr_4$ (Br-PrTPP refers to (3-bromopropyl) triphenylphosphonium) *via* a facile saturated crystallization method.[87] Attributed to the tetrahedrally coordinated $[MnBr_4]^{2-}$ polyhedron, it demonstrates an excellent LY of up to 68 000 photons per MeV and lowest detection limit of 45 nGy_{air} s^{-1}. Li *et al.* prepared 0D $(BTPP)_2MnBr_4$ (BTPP refers to benzyltriphenylphosphonium) as a promising scintillator with excellent air and radiation stability, which showed an appreciable LY of 53 000 photons per MeV, a low detection limit of 89.9 nGy_{air} s^{-1} and an ultra-low afterglow comparable to the commercial BGO single crystal.[88] Furthermore, after fabricated as a flexible screen combined with PDMS, a rather high spatial resolution of 14.1 lp mm^{-1} was achieved. In addition, Gong *et al.* presented a novel group of 0D hybrid manganese halides of A_2MnBr_4 (A = BzTPP, Br-BzTPP, and F-BzTPP).[89] Benefiting from near-unity PLQY, these hybrids show a state-of-art LY of 80 100 photons per MeV for hybrid manganese halides. The 30 nGy_{air} s^{-1} ultra-low detection limit, 14.06 lp mm^{-1} qualified spatial resolution and 0.3 ms short afterglow make it a promising scintillator for further applications.

Apart from all these copper-free scintillators mentioned, there are still several noteworthy studies we would like to present. For example, Wang *et al.* discovered the introduction of a small amount of Sb^{3+} into the indium halide DMA_4InCl_7, resulting in DMA_4InCl_7:10%Sb^{3+}, largely enhancing the PLQY by 9-fold, which originated from efficient energy transfer between Sb^{3+} ions and STE states.[90] The STE emission yields a high LY of 23 500 photons per MeV and a low detection limit of 175 nGy_{air} s^{-1}. Likewise, Huang *et al.* discovered the novel influence of the A-site on the band-edge structures and optoelectronic properties, and some Sb^{3+}-doped 0D halide perovskite derivatives were designed as experimental proof.[91] Benefiting from the deformation of the lattice brought about by Sb^{3+}, STE states are harnessed properly (Fig. 4f), resulting in a qualified LY of up to 60 976 photons per MeV and a detection limit of 90 nGy_{air} s^{-1}. Moreover, Wang *et al.* designed and synthesized a molecular hybrid perovskite, $TpyBiCl_5$, which managed to circumvent thermal quenching *via* multi-excited state switching, originating from the inter-reaction among its counterparts in the perovskite.[92] It also shows a rigid framework structure, resulting in 12 times higher PLQY than its organic ligand (Tpy) at room temperature. $TpyBiCl_5$ maintains an ideal detection limit of 196.31 nGy s^{-1} even at 353 K through thermally activated delayed fluorescence (TADF), and a clear image at 413 K, effectively addressing potential annealing issues observed in other films. This characteristic offers a promising solution for the application of scintillators under extreme conditions, such as *in situ* imaging of thermal loss during mechanical operation. Furthermore, Wang *et al.* synthesized $Ag_6S_6L_6$ (SC-Ag) metal clusters through a simple solvothermal reaction.[93] The heavy atom guarantees an effective TADF mechanism, and satisfyingly, SC-Ag demonstrates a high PLQY of 91.6% and a LY of 17 420 photons per MeV, along with a preeminent spatial resolution of 16 lp mm^{-1}. Additionally, the rigid core structure endows SC-Ag with strong resistance to humidity and radiation. Additionally, Yuan *et al.* pioneered high-performance TADF Ag-based scintillators, namely $Ag_2Cl_2(dppb)_2$ (dppb refers to 1,2-bis(diphenylphosphino)benzene), with an exceptionally high RL intensity and a low detection limit of 59.8 nGy s^{-1}.[94] Its superior performance, compared to the Cu series, mostly results from effective utilization of high excitons due to a small singlet–triplet energy gap. The flexible film fabricated has a high spatial resolution of 25 lp mm^{-1} (Fig. 4g). Another work worth mentioning is that of O'Neill *et al.* who synthesized and characterized $Cs_2Ag_{0.6}Na_{0.4}In_{0.85}Bi_{0.15}Cl_6$ (CANIBIC), an inorganic mixed-cation double halide perovskite, and figured out its STE emission mechanism.[95] Moreover, the CANIBIC-PMMA film demonstrates higher X-ray luminescence intensity than that of

the pure pressed pellet of CANIBIC. Also, Wang *et al.* reported a Mn^{2+}-activated all-inorganic 2D layered Ruddlesden–Popper perovskite, namely Cs_2CdCl_4:10%Mn.[96] It possesses a bright orange–red emission with 90.47% PLQY, strong X-ray absorption, an ultra-high LY up to 88 138 photons per MeV and 31.04 nGy_{air} s^{-1}. A 15 cm × 15 cm flexible screen was prepared by combining PDMS with Cs_2CdCl_4:10%, with a high spatial resolution of 16.1 lp mm^{-1} and qualified imaging capability under an extreme low dose of 16 μGy_{air} s^{-1}.

While copper-free scintillators, as a subclass of their lead-free counterparts, enable elements with analogous elements, such as Mn, Bi, and Te, to better manifest their intrinsic properties for optimizing spectral characteristics and enhancing performance, critical challenges persist. These include the generation of toxic species from undesired byproducts during the synthesis of organic components in hybrid organic–inorganic systems, inherent parity-forbidden transitions in double perovskites necessitating additional strategies to improve the LY,[97] and the hygroscopic nature of lead-free variants imposing stringent encapsulation requirements that limit their practical deployment.[98]

3.2.2 Copper-based scintillators. Cu substitution is the best accepted solution, and $Cs_3Cu_2I_5$ is a widely reported Cu-based scintillator with prominent feasibility, because the zero-dimensional (0D) structure of $Cs_3Cu_2I_5$ effectively localizes and segregates multiple STEs, thereby mitigating Auger recombination.[99] Several works have been reported on this appealing material;[100] here we focus only on work from recent years, for which researchers have focused their efforts on synthesis procedure progress or property enhancement. For instance, to avoid lattice distortion caused by heteromorphic homologs in vacuum-evaporated metal halides (MHs), Peng *et al.* brought out a single-source vacuum evaporation method.[101] A ~10 μm thick film of Cu-MHs was synthesized by using this very strategy, to achieve an impressive LY of 53 983 photons per MeV and a spatial resolution of 14.1 lp mm^{-1}.

Doping is recognized as a potential method for enhancing efficiency and stability. For example, Wang *et al.* focused their efforts on multi-self-trapped excitons of $HCOO^-$-doped $Cs_3Cu_2I_5$ single crystals with transient and steady-state spectroscopy, and figured out that it derived from the host lattice and external dopants separately, which could both be triggered independently.[102] Then, after carefully tuning the excitation wavelength and selectively exciting different STEs, $Cs_3Cu_2I_5$:$HCOO^-$ demonstrates a remarkable PLQY of 99.01% and little self-absorption, with LY being improved by 5.4 times, compared to that of pristine $Cs_3Cu_2I_5$ crystals, up to 61 500 photons per MeV (Fig. 5a). Also, like the lead-based perovskite scintillators, combination with poly-carriers is considered a way of enhancing stability. To illustrate this, Moon *et al.* reported novel technology that integrated $Cs_3Cu_2I_5$ perovskite nanoparticles into densified–delignified wood, namely $Cs_3Cu_2I_5$@D-Wood, for an eco-friendly and biodegradable X-ray scintillator film with a spatial resolution of 10 lp mm^{-1}.[103] Similarly, Hao *et al.* developed an innovative integration of $Cs_3Cu_2I_5$ with PVDF and PMMA, effectively preventing agglomeration and ensuring a more uniform size distribution, which, in turn, improved stability.[104] The as controlled flexible scintillator film displays a satisfying spatial resolution of 14.3 lp mm^{-1} and a low detection limit of 105 nGy s^{-1} was achieved.

To further exert the functionality of $Cs_3Cu_2I_5$ and its derivatives, some praiseworthy investigations have been conducted. For instance, considering that the absence of X-ray energy distinction shall result in insufficient image contrast, Ran *et al.* presented an innovative multi-energy X-ray linear-array detector based on $Cs_3Cu_2I_5$ (Fig. 5b).[105] Benefiting from the negligible self-absorption of the material and side-illuminated scintillation scenarios, the incident X-ray spectra could be reconstructed by analyzing the distribution of the scintillator intensity while illuminated from the side. As a result, the outcome error can be controlled to be below 5.63%. Xiang *et al.* presented centimeter-sized $Cs_3Cu_2Cl_5$ *via* a slow-cooling method, and the planar orientation, which was controlled in a space-confined chamber, required no further shaping before being fabricated as a scintillation screen.[106] The synthesized $Cs_3Cu_2Cl_5$ single crystal exhibits an impressive LY of up to 95 000 photons per MeV and a low detection limit of 2.7 μGy_{air} s^{-1}. Moreover, it could retain its original phase for 6 months in a vial after the surface passivation procedure. Intriguingly, Ran *et al.*, the same group mentioned above, also discovered a better match between $CsCu_2I_3$, once considered the oxidation product, and the spectral responsivity of regular flat-panel photodiode arrays than $Cs_3Cu_2I_5$, showing potential extension for further application in X-ray scintillators.[107]

Another interesting and noteworthy Cu-based scintillator was presented in recent years, and has attracted attention in the frontier research field, namely $Cs_5Cu_3Cl_6I_2$. Its presenters, Wu *et al.*, discovered it possessed benign grain boundaries without dangling bonds, which were commonly considered to contribute to RL lifetime extension and nonradiative recombination loss increase.[108] After fabrication as a columnar morphology *via* close space sublimation, it exhibits negligible afterglow and a high LY (Fig. 5c). The imaging property was also determined; it demonstrated a spatial resolution of 27 lp mm^{-1} with a frame rate up to 33 fps. Also, Zhang integrated a $Cs_5Cu_3Cl_6I_2$ event-based scintillator film with negligible ghosting artifacts (0.1%) and an impressive data compression ratio of 23.7%.[109] Shu *et al.* reported the Rb doped $Cs_5Cu_3Cl_6I_2$ crystal with considerable improvement in stability against heat and humidity and an outstanding LY.[110] Combined with PDMS, the $Cs_5Cu_3Cl_6I_2$:Rb scintillator screen reaches a high spatial resolution of over 10 lp mm^{-1}.

Besides, copper(I) itself can also be used as a dopant to enhance the STE state. To illustrate, Hu *et al.* discovered that the introduction of 0.05% Cu^+ into Rb_2AgBr_3:Cu^+ could largely enhance the PLQY to 98.8% (Fig. 5d).[111] Consequently, a pre-eminent LY of 79 250 photons per MeV and rather low detection limit of 714.83 nGy s^{-1} were achieved. Likewise, Yao *et al.* synthesized 1D Cu^+-doped Rb_2AgI_3 with 76.48% PLQY, demonstrating a LY of 36 293 photons per MeV, a low detection limit of 1.022 μGy_{air} s^{-1} and a decay time of 465 ns.[112] In very recent

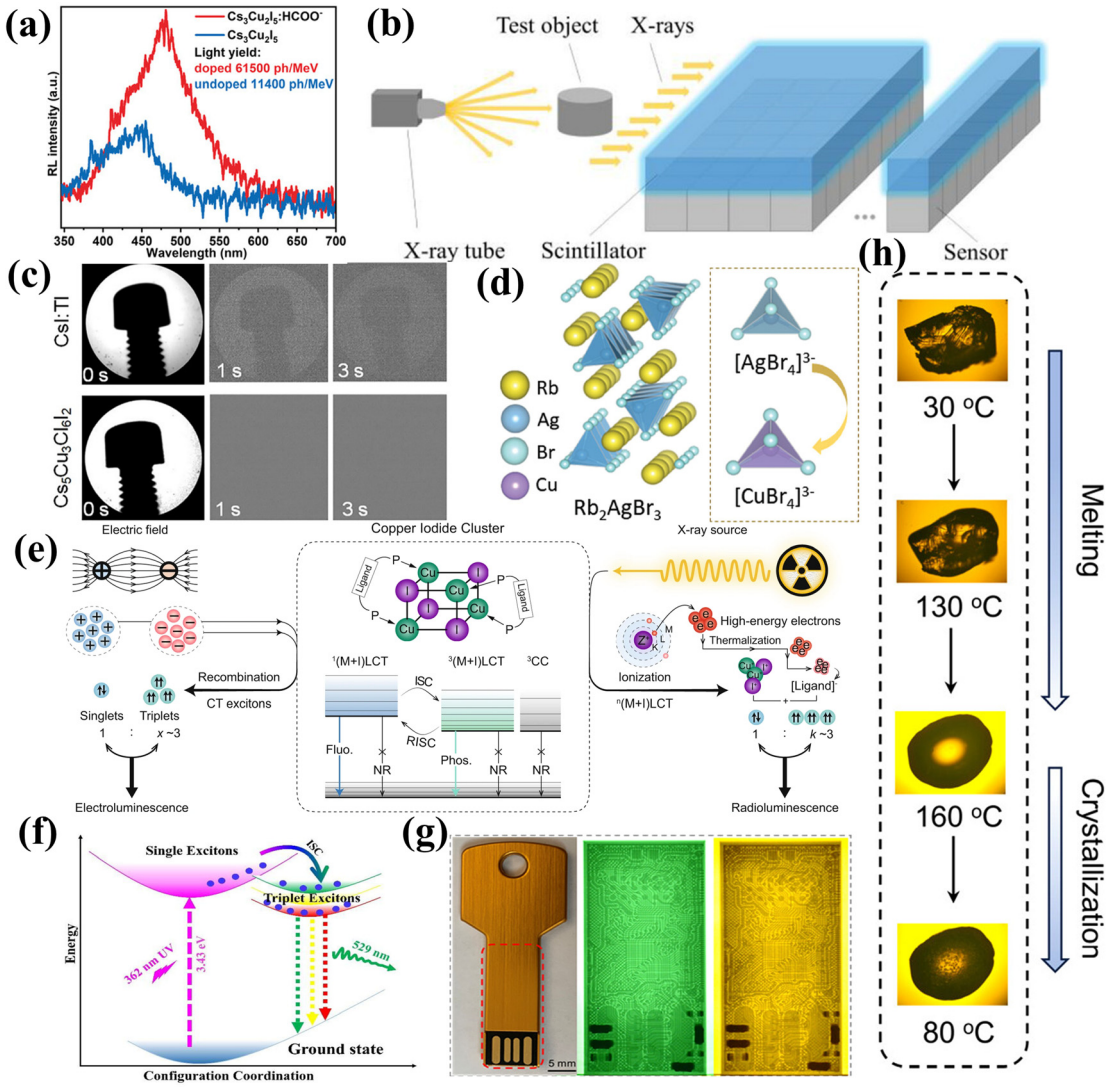

Fig. 5 (a) RL spectra of pristine and $HCOO^-$-doped $Cs_3Cu_2I_5$ single crystals. (b) Schematic of SIXS for multi-energy X-ray detection and imaging. (c) Dynamic imaging of a screw after 10 s of X-ray excitation using CsI:Tl and $Cs_5Cu_3Cl_6I_2$ films. The $Cs_5Cu_3Cl_6I_2$ film shows no residual image, while the image in the CsI:Tl film persists even after 3 s. (d) Crystal structure diagram of Rb_2AgBr_3 (left) and the schematic substitution model *via* Cu^+ doping (right). (e) Schematic of the mechanisms in Cu_4I_4 cubic clusters. (f) The PL mechanism in the configuration coordinate diagram of $[BzTPP]_2Cu_2I_4$. (g) Bright-field and X-ray images of a USB drive. (h) POM images of M_3 at different temperatures.

work, Wu *et al.* further enhanced the performance of Rb_2AgBr_3:Cu^+, achieving single crystals with a PLQY of up to 99.2%.[113] Through pulsed decay measurements and DFT calculations, they demonstrated that the incorporation of Cu increased the density of deep bound excitons, thereby significantly enhancing radiative recombination. By integrating the material with PDMS, they successfully fabricated a large-area flexible scintillator film, which exhibited a spatial resolution of 10.2 lp mm^{-1}, indicating its potential applications in radiation monitoring and biomedical imaging.

Copper-based systems, serving as a viable substitute for their lead-containing counterparts, have emerged as one of the most promising non-toxic scintillator candidates. Nevertheless, even though elemental doping strategies have been employed to mitigate their degradation under ambient conditions, the degradation pathways, such as oxidation or segregation remain non-negligible.[114] Furthermore, the spectral mismatch between their emission profile and the responsivity spectra of commercially available photodetectors imposes additional constraints on achieving optimal detection efficiency.[115]

3.3 Cu-based cluster scintillators

Another huge family of Cu-based scintillator materials are Cu_xI_x clusters, usually combined with organic cations or polymers, which no doubt are emerging as new X-ray scintillators (Table 3). Blessed with double STE emission, these clusters usually exhibit a considerable LY, a large Stokes shift and high-

Table 3 The parameters of Cu-based cluster scintillators

Material	Type	Light yield (photons per MeV)	Detection limit (nGy_{air} s^{-1})	Spatial resolution (lp mm^{-1})	Ref.
$Cu_4I_6(bttmpe)_2$	Cluster	—	—	17	117
$Cu_6I_8(bu\text{-}ted)_2$	—	—	19.6	20	118
$(IPP)CuI_2$	Cluster	75 793.83	62.29	10.2	119
$(C_{12}H_{28}N)_2Cu_2I_4$	Single crystal	56 000	28.39	19.8	120
$[DDPACDBFDP]_2Cu_4I_4$	Cluster	—	77	12	121
$Cu_4I_4(C_6H_{14}N_2)_2$	3D	48 538	30.68	—	122
$Cu_2I_2(3,4\text{-}DMP)_4$	0D	38 031	106.71	10	123
$(18\text{-crown-}6)_2Na_2(H_2O)_3Cu_4I_6$ (CNCI)	0D	109 000	59.4	16.3	124
$(BzTPP)_2Cu_2I_4$	0D	27 706	352	4.928	125
$(CISDM)_4[Cu_4I_8]$ $_2H_2O$	2D	41 042	86.8	108	126
$(4\text{-bzpy})_4Cu_4I_4$	0D	60 948	155.2	5	127
$TPA_2Cu_2I_4$	0D	40 124	126	5.5	128
$Cu_4I_6(L1)_2$	0D	32 600	96.4	30	129
$(MTP)_2CuI_3$ (M1)	0D	6400	72.6	20	130
$Cu_6I_8(bu\text{-}ted)_2$	—	—	32	17	131
1-rod	MOF	41 000	34.6	20	132
$Cu_4I_4(R_3As)_3L$	Cluster	15 000	18.1	—	133
Cu_2X_2 (X = Cl, Br and I)	Nanoclusters	175 000	—	30	134
$[CuI(PPh_3)_2R]$ (R = PH, Cu-1 or PH-Br, Cu-2)	Cuprous complex	—	49.7	6.8	135

efficiency white light emission.[116–118] As a highly regarded material, major efforts have been reported. For instance, Lai *et al.* prepared organic cuprous iodide clusters, $(IPP)CuI_2$ (IPP refers to iso-propyltriphenylphosphonium).[119] These present the best scintillator property when IPP : CuI = 1 : 0.75, with a super low detection limit of 62.29 nGy s^{-1} and an ultrahigh LY of 75 793.83 photons per MeV. They also applied it to CT and obtained a clear reconstructed 3D model, due to its superior spatial resolution of 10.2 lp mm^{-1}. Zhao *et al.* designed and fabricated a novel metal halide scintillator, $(C_{12}H_{28}N)_2Cu_2I_4$, with white emission.[120] Benefitting from the double self-trapped mechanism, it demonstrates a really high PLQY, which not only matches with the response of semiconductor-based sensors, but also decreases the doses to which the objects are exposed. The flexible transparent large-area scintillator film made from this shows a superior luminescence property, a high spatial resolution of 19.8 lp mm^{-1} and an incredibly low detection limit of 28.39 nGy_{air} s^{-1}; these values are four times higher and 194 times lower than the typical value in medical usage. Moreover, recognizing the trivial factor that X-ray luminescence efficiency in metal clusters is governed by the competition between radiative states from organic ligands and non-radiative ones (Fig. 5e), Zhang *et al.* reported a class of Cu_4I_4 cubes, including $[DDPACDBFDP]_2Cu_4I_4$ (DDPACDBFDP refers to 10,10′-(4,6-bis(diphenylphosphanyl))). It presents an impressive emissive RL due to functionalizing the biphosphine ligands with acridine, which can effectively absorb ionization radiation to generate electron–hole pairs and subsequently transfer them to ligands during thermalization.[121] It demonstrates a PLQY of 95%, benefiting from triplet-to-singlet conversion *via* a TADF matrix, the lowest detection limit of 77 nGy s^{-1} and a high spatial resolution of up to 12 lp mm^{-1}. Similarly, Zou *et al.* employed a solvent-recyclable green process to synthesize stable three-dimensional nanoclusters, $Cu_4I_4(C_6H_{14}N_2)_2$, achieving a PLQY close to 100%.[122] The sturdy 3D framework ensures the morphological stability of the molecules at high temperatures and humidity. It retains 90% of its room-temperature luminescence intensity at 110 °C and 88.34% of its initial luminescence intensity after 100 days under ambient conditions. This demonstrates a promising approach for the green, low-toxicity synthesis of high-performance, lead-free nanoclusters. In work recently reported by the same group, Zou *et al.* synthesized hybrid copper iodide single crystals, $Cu_2I_2(3,4\text{-}DMP)_4$ (3,4-DMP = 3,4-dimethylpyridine), with a PLQY of 80%, utilizing ionic liquids as both the solvent and iodine source, and nitrogen-containing organic ligands for structural modulation.[123] Notably, the material overcomes the common issue of moisture-induced degradation, demonstrating exceptional stability over 90 days, thereby providing a novel solution for the inkjet printing of scintillators.

To extend the scintillator properties, Wang *et al.* synthesized $(18\text{-crown-}6)_2Na_2(H_2O)_3Cu_4I_6$ (CNCI) with little self-absorption and near-unity green light emission.[124] It possesses the highest values of LY ever reported, up to ~109 000 photons per MeV, and other impressive scintillator properties, like an ultralow detection limit of 59.4 nGy s^{-1} and an appreciable spatial resolution of 16.3 lp mm^{-1} for CNCI–polymer film screens, which are further improved after modification by a silicon wave guide structure to 24.8 lp mm^{-1}. Furthermore, Lin *et al.* designed $(BzTPP)_2Cu_2I_4$ (BzTPP refers to benzyltriphenylphosphonium) as a scintillator, exhibiting a substantial Stokes shift of 167 nm and 27 706 photons per MeV, the energy transfer mechanism of which is shown in Fig. 5f. This material stands out as the premier choice among copper-based scintillators.[125] Also, Yang *et al.* presented a 2D-copper-based cluster, $(CISDM)_4[Cu_4I_8]$ $2H_2O$ (CISDM refers to *cis*-2,6-dimethylmorpholine), as a qualified scintillator material, with 87.2%

PLQY at 588 nm.[126] It also demonstrates a strong linear response to X-rays, with a LY of 41 042 photons per MeV, a low detection limit of 86.8 nGy s^{-1}, and an exceptional resolution of 108 lp mm^{-1}. These characteristics represent a state-of-the-art performance for lead-free metal halide hybrid materials in spatial detection. Also, Kong *et al.* combined a conjugated organic cation (4-benzylpyridine, 4-bzpy) with copper(I) iodide modules to grow organic copper halide single crystals, namely 0D cubane-like $(4\text{-bzpy})_4Cu_4I_4$.[127] It demonstrates a high LY of 60 948 photons per MeV and an exceptional linear relationship with X-ray dose, originating from the ligand-to-core charge transfer state. Similarly, Lv *et al.* developed a copper halide scintillator, $TPA_2Cu_2I_4$, utilizing the principle of STE ultra-broadband emission.[128] The material achieves a remarkably high PLQY of 94.27%, a LY of 40 124 MeV^{-1}, and a spatial resolution of 5.5 lp mm^{-1}, thereby providing new insights into broadband-emission X-ray scintillators.

Also, a nano-rod strategy was employed to promote the performance. He *et al.* chose copper iodide ink, $Cu_4I_6(L_1)_2$ (L_1 refers to 1-propyl-1,4-diazabicyclo[2.2.2]octan-1-ium) 0D nanorods, as the scintillator, which exhibited a PLQY of 95.3% for broadband green emission, and the imaging result of this scintillator film is shown in Fig. 5g.[129] The subsequent scintillator screen shows a low detection limit of 96.4 nGy s^{-1}, approximately 55 times lower than that required for standard medical diagnosis (5.5 μGy s^{-1}). Furthermore, the spatial resolution exceeding 30 lp mm^{-1} was twice that of conventional scintillators. To enhance the stability, Bohan Li *et al.* fabricated three excellent glass phase 0D hybrid copper halides, $(MTP)_2CuI_3$ (M_1) (MTP refers to methyltriphenylphosphonium), $(MTP)_2Cu_4I_6$-α (M_2)′$(MTP)_2Cu_4I_6$-β (M_3), which shared the same inorganic anions.[130] The prepared glass samples were heated in air to promote the crystal–glass phase transition, and the self-assembly enabled recrystallization, resulting in a hybrid bulk glass-ceramic; the procedure is illustrated by polarized optical microscopy (POM), as shown in Fig. 4h. It demonstrates an outstanding LY of 64 000 photons per MeV, a detection limit of 72.6 nGy s^{-1} and high stability for real-time X-ray imaging with spatial resolution above 20 lp mm^{-1}.[130] Likewise, Gu *et al.* reported the synthesis of $Cu_6I_8(\text{bu-ted})_2$ *via* a surfactant-assisted method, limiting the crystal size with the help of controlling surface tension.[131] The material shows a near-unity PLQY, resulting in a light output 4.8 times higher than that of the commercial scintillator $Lu_3Al_5O_{12}:Ce^{3+}$, as well as an impressively low detection limit of 32 nGy s^{-1} and a spatial resolution of 17 lp mm^{-1} while integrating SDBS into a flexible screen. Also, for the purpose of preparing a high quality, flexible and stable scintillator screen, Peng *et al.* selected a macrocyclic bridging ligand with an aggregation-induced emission feature as the MOF, which could endow the scintillator with high efficiency and preeminent stability, combined with a copper iodide cluster.[132] The as-fabricated scintillator film exhibits exceptional flexibility, enabling their integration with flexible OLEDs for the precise imaging of complex surfaces or internal structures of objects. This capability holds significant potential for applications in industrial inspection and biological imaging. Moreover, the introduction of *in situ* polyvinyl pyrrolidone during the synthesis process leads to the regular rod-shaped microcrystal, enhancing the processibility even further. The scintillator realizes dynamic X-ray flexible imaging for the first time with a real time ultra-high spatial resolution of 20 lp mm^{-1}. Also, Demyanov *et al.* presented cubane Cu_4I_4–triarsenic clusters $[Cu_4I_4(R_3As)_3L]$ (R refers to the organic functional group, L refers to no ligand or nitrile) with a record ultralow detection limit of 18.1 nGy s^{-1} and an exquisite linear response over a wide range of X-ray doses (0–640 μGy_{air} s^{-1}).[133] Yuan *et al.* reported their discovery that Cu_2X_2 (X = Cl, Br and I) was a TADF nano-cluster scintillator suffering from no mechanochromism and blessed with a considerable X-ray absorption cross section, which contributed to a flexible scintillator screen with excellent radiation and humidity resistance, an ultra-high LY of 175 000 photons per MeV and a high spatial resolution of ~30 lp mm^{-1}.[134] Besides, for the purpose of being eco-friendly, Chen reported a mechanochemical method for synthesizing $[CuI(PPh_3)_2R]$ (R = PH, Cu-1 or PH-Br, Cu-2), circumventing the harm brought by diverse organic solvents in traditional chemical experiments.[135] Cu-2 demonstrates 2.52 times higher RL intensity than that of the commercial BGO scintillator and 1.52 times larger than that of Cu-1 due to the introduction of PH-Br, which resulted in 37.75% higher PLQY.

Nanoclusters, emerging as a novel class of materials with dimensions intermediate between single atoms and quantum dots, exhibit near-unity PLQY and negligible Stokes shifts. However, key mechanistic aspects, such as the nature of halide ligand coordination dynamics, remain elusive,[127] while their prevalent mechanochemical grinding synthesis protocols face scalability challenges compared to solution-based methods commonly employed for other luminescent materials.[136]

3.4 Rare-earth nanocrystalline scintillators

Rare-earth-doped scintillator materials demonstrate promising applications in nuclear medicine, radiographic imaging, encryption and particle detection. The high energy-transfer efficiency among rare-earth elements enhances the overall performance of the materials, yielding greater light output. Furthermore, doping with rare earth elements enhances the thermal and chemical stability of scintillator materials. Their unique properties also enable a wide range of luminous wavelengths, meeting the diverse needs of various applications.[137]

In recent efforts, the doping of rare-earth elements into perovskite materials has yielded significant progress. For instance, in 2024, Wang *et al.* reported a series of $Cs_2Ag_xNa_{1-x}In_yBi_{1-y}Cl_6$ halide scintillators doped with rare-earth ions.[138] Among them, $Cs_2Ag_{0.6}Na_{0.4}In_{0.95}Bi_{0.05}Cl_6$:5%Tm has a high PLQY in NIR light of up to 76.3% and a LY of up to 33 500 photons per MeV. The flexible scintillators achieved a high spatial resolution of 11.2 lp mm^{-1} and a low X-ray detection limit of 55.2 nGy_{air} s^{-1}. Moreover, after doping with Tm ions, they achieved clear imaging under bright external lighting by using an infrared camera with a 760 nm long-pass filter in front of the lens (Fig. 6a).

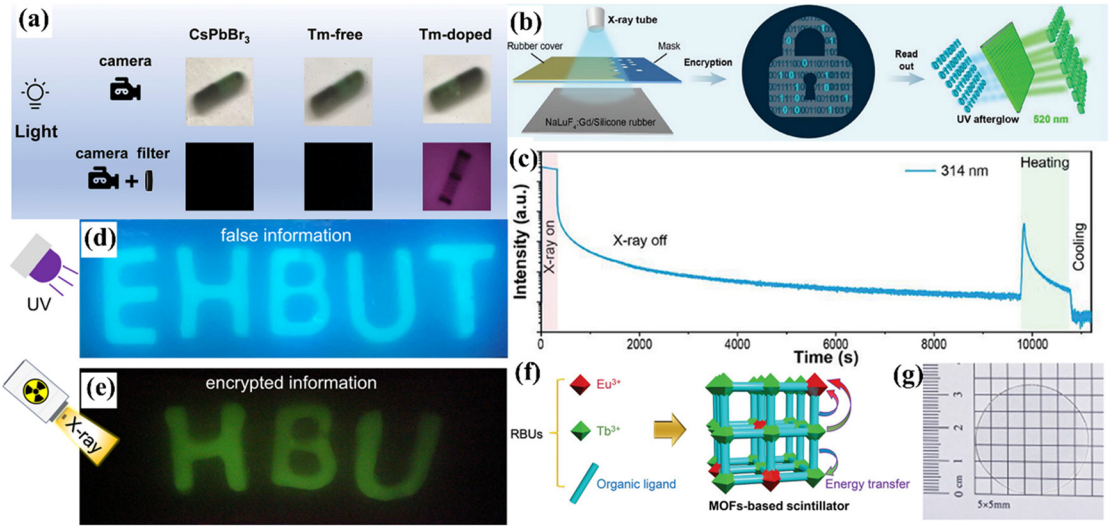

Fig. 6 (a) X-ray images of encapsulated springs under various conditions were captured using $CsPbBr_3$, $Cs_2Ag_{0.6}Na_{0.4}In_{0.95}Bi_{0.05}Cl_6$ (Tm-free), and $Cs_2Ag_{0.6}Na_{0.4}In_{0.95}Bi_{0.05}Cl_6$:5%Tm (Tm-doped) films. (b) Schematic diagram of writing X-ray imaging information and decryption by a layer of the perovskite nanocrystals. (c) Decay curve of the thermal-stimulated luminescence of $NaLuF_4:Gd^{3+}$ (20 mol%) at 314 nm was recorded at room temperature after X-ray excitation was stopped for 5 min. The film was then heated to 80 °C for 160 min. (d) Photograph of the false information EHBUT in the prepared multilayer hydrogel under UV light (365 nm). (e) Photograph of the encrypted information HBU in the multilayer hydrogel after exposure to X-rays. (f) Schematic representation of radio-luminescent functional building units for constructing a thermo-responsive MOF scintillator. (g) Bright field photograph of glass scintillators.

Doping rare-earth ions into fluoride-containing nano-scintillators is also a recognized approach.[8,139–144] In 2023, Yang *et al.* reported high-security X-ray imaging encryption technology by developing an ultra-long RL memory film, namely $NaLuF_4:Gd^{3+}$ or Ce^{3+}, which captured subtle pure UV emission characteristics.[145] The encrypted X-ray imaging information can be securely stored in memory films for over seven days and can be optically decoded using perovskite nanocrystals (Fig. 6b and c). Moreover, the as-fabricated flexible memory film exhibits a high spatial resolution of 20 lp mm^{-1}. The varying durations of fluorescence lifetime offer distinct advantages in different application contexts. To address the issue of strong hysteresis scintillation luminescence, Zhang *et al.* synthesized $LiYF_4$:15Tb/25Gd@$LiYF_4$ core/shell nano-scintillators to inhibit the generation of Frenkel defects.[141] In the same year, Yang *et al.* reported $NaLuF_4$:Gd/Tb/Eu doped with 5%Tb with a high LY of 15 313 photons per MeV and a low detection limit of 84.1 nGy_{air} s^{-1}.[146] Subsequently, Zhang *et al.* exhibited Tb^{3+}-doped $Na_5Lu_9F_{32}$ with good water dispersibility and highly sensitive luminescence to X-rays.[147] Remarkably, they employed multilayer hydrogels for information camouflage and multilayer encryption. The encrypted information can only be identified through X-ray exposure, while false information is revealed under ultraviolet light (Fig. 6d and e). In 2024, Lu *et al.* proposed a type of heterovalent Cu^{2+} ion co-doped $LiLuF_4$:Tb,Cu microcrystalline scintillation material with higher RL intensity, long afterglow and thermoluminescence intensity.[148] The detection limit of $LiLuF_4$:Tb,Cu can reach 2.7928 nGy s^{-1} and a spatial resolution of 22 lp mm^{-1}@MTF = 0.2 is achieved.

In the field of scintillators materials, MOFs provide a tunable platform for the integration of X-ray absorption centers and luminescent chromophores in a dense framework manner and rare-earth-doped MOFs are widely studied recently, as it is in perovskite scintillators.[149] In 2024, Li *et al.* proposed thermo-responsive lanthanide MOF scintillators ($Tb_{0.95}Eu_{0.05}$-BPTC), presenting a low dose rate detection limit of 156.1 nGy_{air} s^{-1} (ref. 150) (Fig. 6f). $Tb_{0.95}Eu_{0.05}$-BPTC has a high relative LY of 39 000 photons per MeV, imaging spatial resolution of 18 lp mm^{-1}, good irradiation stability and giant color transformation visualization, benefiting the applications. Similarly, Jin *et al.* reported [1-ethyl-3-methylimidazolium] $EuBr_3$MeOH as scintillators with a LY of 43 000 ± 100 photons per MeV and achieved spatial resolution above 10 lp mm^{-1}.[151] Additionally, Yang *et al.* reported Eu-pba and Tb-pba, featuring excellent radiation, hydrolytic, and thermal stabilities. Using them as scintillators can result in a linear response to the X-ray dose rate with detection limits of 4.92 and 3.17 μGy s^{-1}, respectively.[152] Recently, Xu *et al.* firstly proposed organo-lanthanide scintillators that offered diverse emission colors from ultraviolet to near-infrared and enabled precise control of luminescence lifetimes from nanoseconds to microseconds.[153] Their materials can efficiently capture the dark triplet excitons generated during the absorption of secondary X-rays, leading to the production of highly stable and efficient RL that surpasses those of commercialized scintillators. Among these scintillators, for instance, remarkably, $Eu(NTA)_3$DPEPO (where NTA refers to 4,4,4-trifluoro-1-(2-naphthyl)-1,3-butanedione and DPEPO refers to bis(2-(diphenylphosphino)phenyl) ether oxide) showed a more than 1000-fold enhancement in RL com-

pared with $EuCl_3$ salts with an equal molar amount of Eu^{3+}. In a recent study, Wang *et al.* reported the successful synthesis of a novel terbium-based MOF (Tb-MOF-1), the enhanced RL performance of which was attributed to the efficient sensitization effect of the $HDOBPDC^{3-}$ ligand.[154] This material demonstrated a remarkably low X-ray detection limit of 1.71 μGy s^{-1}, significantly surpassing conventional scintillation thresholds. Furthermore, the researchers developed a flexible composite scintillator screen through polymer matrix integration, which exhibited exceptional imaging capabilities with a spatial resolution of 7.7 lp mm^{-1}, meeting clinical radiography requirements.

Rare-earth-doped glass scintillators have also attracted significant attention in recent years due to outstanding optical performances such as high transmittance (Fig. 6g) and their ability to absorb high energy radiation and convert the energy into visible light.[155,156] In 2023, Sun *et al.* fabricated Tb^{3+}-doped and Ce^{3+}/Tb^{3+}-co-doped oxyfluoride scintillator (C_4T_9) glass samples with a spatial resolution of 16 lp mm^{-1}.[157] Then in 2024, Li *et al.* synthesized Tb^{3+}-doped oxyfluoride aluminosilicate glass scintillators with a spatial resolution of 20 lp mm^{-1} and higher RL of up to 224% compared to the $Bi_4Ge_3O_{12}$ crystal.[158] Subsequently, Dai *et al.* reported a transparent glass-ceramic scintillator by embedding Tb^{3+}-doped $NaLu_2F_7$ nano-crystals in a glass matrix.[159] Importantly, most decreases in performance, due to prolonged exposure to high doses of X-rays, can be completely restored by heat treatment at 350 °C for 30 min.

Additionally, several other rare-earth-doped scintillators have been reported.[160,161] For instance, in 2023, Ling *et al.* prepared YF_3:30%Gd^{3+}/10%Tb^{3+} micro-particles with fine environmental stability and superb X-ray RL, which achieved an imaging spatial resolution of 16.8 lp mm^{-1}.[162] Subsequently, in 2024, Wang *et al.* reported zero-thermal-quenching $Lu_3Al_5O_{12}:Ce^{3+}$ transparent ceramics (0.5 mm) with excellent spatial resolution of up to 112 lp mm^{-1}.[163] In the same year, Yang *et al.* synthesized single crystals of rare earth ion-doped ternary chalcogenides, $NaGaS_2$/Eu, with a low detection limit of 250 nGy s^{-1} and a spatial resolution of 13.2 lp mm^{-1}.[164] Doping with rare-earth elements imparts some materials with unexpectedly excellent properties, making the continued exploration of the potential of rare-earth-doped scintillators very promising. Furthermore, Wang *et al.* recently advanced the frontier of high-temperature scintillator technology through the development of a Tb^{3+}-doped nanocrystalline glass composite system.[165] This material possesses a record LY of 54 900 photons per MeV and a sensitivity of 635.31 nGy_{air} s^{-1}. Remarkably, the material maintains exceptional thermal stability with 28.1 lp mm^{-1} spatial resolution at 500 °C and robust moisture resistance, surpassing current high-temperature scintillators.

The utilization of rare earth elements in optical materials has been extensively investigated (Table 4), as their intricate electronic configurations offer a compelling avenue for tailoring material band structures. However, the environmental and biological implications of these elements demand critical scrutiny, as exemplified by nephrotoxicity associated with gadolinium exposure, pulmonary fibrosis risks linked to samarium compounds,[166] and inflammatory responses triggered by elevated cerium concentrations.[167] Furthermore, the strikingly similar physicochemical properties among rare earth elements complicates purification processes, which objectively inflate raw material costs and ultimately constrain their large-scale industrial implementation.

Table 4 The parameters of rare-earth nanocrystalline scintillators

Material	Type	Light yield (photons per MeV)	Detection limit (nGy_{air} s^{-1})	Spatial resolution (lp mm^{-1})	Ref.
$Cs_2Ag_{0.6}Na_{0.4}In_{0.95}Bi_{0.05}Cl_6$:5%Tm	Single crystals	33 500	55.2	11.2	138
$LiYF_4$:15Tb/25Gd@$LiYF_4$	Nanocrystals	—	—	20	141
$NaLuF_4$:Gd/Tb/Eu with 5%Tb-doping	Nanocrystals	15 313	84.1	8.7	146
Tb^{3+}-doped $Na_5Lu_9F_{32}$	Nanocrystals	15 800	—	—	147
$LiLuF_4$:Tb,Cu	Microcrystals	—	2.7928	22	148
$Tb_{0.95}Eu_{0.05}$-BPTC	MOFs	39 000	156.1	18	150
[1-Ethyl-3-methylimidazolium]$EuBr_3$MeOH	Organic–inorganic hybrids	43 000	405.4	>10	151
Eu-pba/Tb-pba	Organic–inorganic hybrids	—	4920/3170	8/12.6	152
$Eu(NTA)_3$DPEPO	Organic–inorganic hybrids	38 589	30.8	20	153
Ln-MOF $[Tb(HDOBPDC)(DMF)(H_2O)]_n$	MOF	—	1710	7.7	154
SiBNaBaGd–*x*Tb	Glass	—	—	20	155
Ce^{3+}-doped $55SiO_2$–$20Al_2O_3$–$15SrF_2$–10NaF	Glass	—	—	18	156
Ce^{3+}/Tb^{3+}-co-doped $55SiO_2$–$14.5SrF_2$–$4.5SrO$–$15LuF_3$	Glass	—	343.9	16	157
$10Al_2O_3$–$0.5Sb_2O_{3-x}Tb_4O_7$–$yCeF_3$ $55SiO_2$–$20Al_2O_3$–$15BaF_2$–10NaF–$xTbF_3$	Glass	—	—	20	158
Tb^{3+}-doped $NaLu_2F_7$	Nanocrystals	—	—	20	159
SrS:Ce^{3+}/CaS:Ce^{3+}	Nanocrystals	—	660		160
$2BaO$–$3SiO_2$ doped with Eu_2O_3	Glass	26 000	—	12	161
YF_3:Gd^{3+}/Tb^{3+}	Microparticles	—	—	16.8	162
$Lu_3Al_5O_{12}:Ce^{3+}$	Ceramics	40 200	—	112	163
$NaGaS_2$/Eu	Crystal	8188	250	13.2	164
$KTb_{3-x}Gd_xF_{10}$	Crystal	54 900	635.31	28.1	165

3.5 Organic scintillators

In addition to the scintillators mentioned above, organic scintillators have garnered significant attention[168–170] due to their rapid response times, diverse chemical structures, low processing temperatures, and cost-effectiveness (Table 5). During the luminescence phase, the charge carriers recombine to produce singlet states (25%) and triplet states (75%), resulting in light emission. However, triplet excitons may be lost due to the dark state characteristics of fluorescent organic scintillators.[171] TADF and room-temperature phosphorescence (RTP) materials have garnered significant attention due to their ability to exhibit bright triplet excitons under X-ray excitation.[172,173] Additionally, hybridized local and charge-transfer (HLCT) excited states in organic donor–acceptor systems can produce efficient PL through high-efficiency triplet–singlet reverse intersystem crossing (RISC) transitions, achieving nearly 100% utilization of excitons.[174] To enhance efficiency and achieve rapid RISC, a common strategy involves increasing the spin–orbital coupling constant (SOC) in organic emitters by exploiting heavy-atom effects.[175] Researchers have proposed innovative methods and applications based on these principles and have identified numerous new, high-performance purely organic scintillators.

The RL performance of organic fluorescence scintillators could be enhanced by improving carrier transport capabilities.[176] Following this guidance, in 2023, Chen *et al.* introduced a highly efficient organic fluorescent scintillator, 4,4′-bis(9-carbazolyl) biphenyl (CBP), which demonstrated a high PLQY of 61.92% and excellent carrier transport ability (Fig. 7a), and biphenyl (BP) showed an average hole mobility of 0.055 $cm^2\ V^{-1}\ s^{-1}$ while CBP achieved a hole mobility of 0.094 $cm^2\ V^{-1}\ s^{-1}$.[177]

In the same year, Chen *et al.* proposed a molecular design strategy that incorporated supramolecular halogen bonding in fluorescence and room-temperature phosphorescence systems containing pyridine rings.[178] Upon exposure to X-ray radiation, the introduction of halogen heavy atoms (X = Cl, Br, I) into 9,10-bis(4-pyridyl)anthracene (BPA) and the formation of halogen bonding interactions in bromophenyl–methylpyridinium iodide (PYI) crystals facilitate the generation of numerous hot electrons and deep holes (Fig. 7b). These charge carriers undergo a series of conversion and transport processes, including electron–electron scattering, Auger processes, and thermalization, resulting in a substantial number of low-energy carriers. Subsequently, these carriers recombined to form electron–hole pairs, leading to the production of 25% singlet and 75% triplet excitons, consistent with spin statistics. During the luminescence process, BPA-X crystals produced rapid fluorescent light emission, primarily utilizing 25% singlet excitons, while PYI crystals exhibited phosphorescent light emission, harnessing both singlet and triplet excitons. Similarly, Chen *et al.* utilized the strategy of incorporating heavy atoms in their latest publication.[179] They developed a new category of organogold(III) complexes, namely Tp-Au-1 and Tp-Au-2, by adopting a through-space interaction motif to achieve high X-ray attenuation efficiency and efficient harvesting of triplet excitons for emission. Gold is a promising transition metal due to its significant spin–orbit coupling constant, derived from its large atomic number (Z = 79) and greater abundance compared to widely used metals like iridium or platinum.[180] Consequently, neat films of Tp-Au-1 and Tp-Au-2 exhibit notable TADF properties with significant triplet–singlet charge transfer features, short decay lifetimes of 1.7–2.2 μs and a high PLQY of up to 77%. Remarkably, the emission mechanism of Tp-Au-1 and Tp-Au-2 can be tuned from TADF to phosphorescence by adjusting the polarity of the host matrix. Under X-ray irradiation, Tp-Au-2 demonstrated intense RL and a record-high scintillation LY of 77 600 photons per MeV for organic scintillators. The resulting scintillator screens provided high-quality X-ray imaging with a spatial resolution exceeding 16.0 lp mm^{-1} (Fig. 7c).

In 2024, Dong *et al.* reported two phenothiazine derivatives exhibiting polymorphism-dependent phosphorescence RL.[181] These derivatives demonstrate high radio stability and a low detection limit of 278 nGy s^{-1}. The study not only introduced sulfur atoms to enhance X-ray absorption through the heavy atom effect but also confirmed that incorporating pyrimidine and pyridine groups containing heteroatoms into the phenothiazine skeleton promoted n–π* transitions, improving the

Table 5 The parameters of organic scintillators

Material	Light yield (photons per MeV)	Detection limit ($nGy_{air}\ s^{-1}$)	Spatial resolution (lp mm^{-1})	Ref.
$Py_2TTz–I_2F_4$	32 583	70.49	26.8	168
$(TPPcarz)_2MnBr_4$	44 600	32.42	—	169
Tetra(*p*-bromophenyl)ethene@poly(vinyltoluene)	14 443	—	13.9	170
4,4′-Bis(9-carbazolyl)biphenyl	—	25.5	14.3	177
BPA-X (X = Cl, Br, I)	—	25.95 ± 2.49	20	178
Tp-Au-2	77 600	—	16	179
10-(Pyridine-2-yl)-10*H*-phenothiazine	—	278	—	181
Sulfone-based organic molecules C_6	16 558	—	15	182
DCB@C[3]A	—	77.1	20	183
BiND-OMe	—	70.68	11	186
OMNI-PTZ 2	—	97	20	187
1,1,2,2-Tetrakis(4-bromophenyl)ethylene	34 600	447	18.69	188

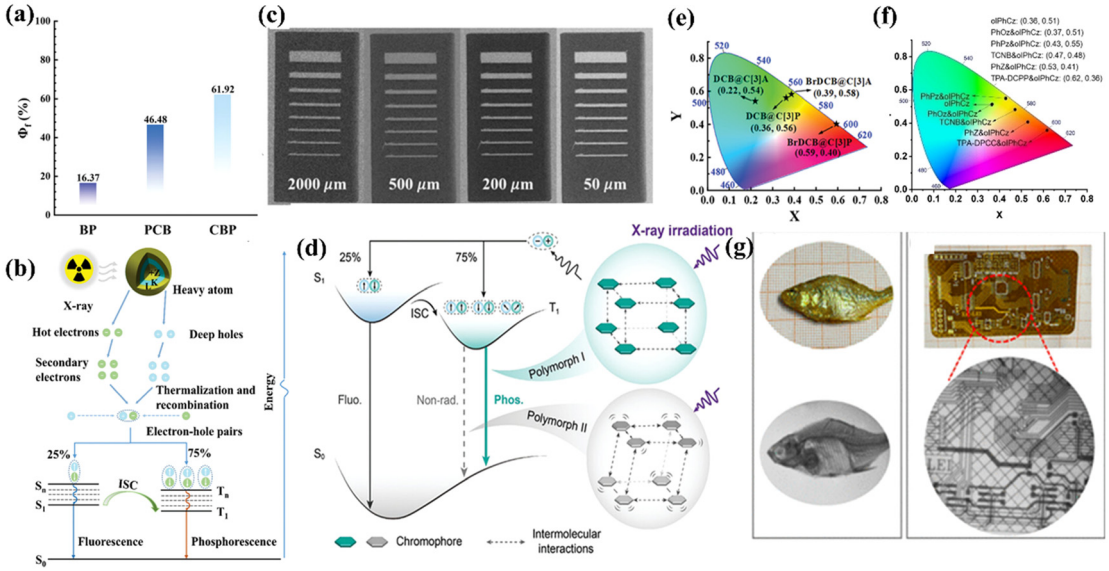

Fig. 7 (a) The PLQYs of BP, PCB, and CPB crystalline powders. (b) A reasonable mechanism of radioluminescence in BPA-X and PYI materials. (c) X-ray images of a standard X-ray test pattern plate of four scintillator screens with different thicknesses of 0.05, 0.2, 0.5, and 2 mm. (d) Organic phosphorescent scintillation processes dependent on polymorphism under X-ray irradiation. (e) Commission Internationale de l'Eclairage (CIE) coordinates calculated from the RL spectra of different materials mentioned in this study. (f) CIE chromaticity coordinate diagram of the RL colors of the host–guest materials. (g) Bright-field images and photographs under X-ray exposure of a fish and an electronic circuit board.

intersystem crossing (ISC) process. Additionally, these groups stabilize triplet excitons, thereby enhancing room-temperature phosphorescence through multiple intermolecular interactions in the crystalline state (Fig. 7d). The experiments reveal that molecule stacking significantly affects the non-radiative decay of the triplet excitons of scintillators, which further determines the phosphorescence scintillation performance under X-ray irradiation. In 2024, Zhan *et al.* adopted a similar approach by developing several proof-of-concept sulfone-based organic molecules (C1–C7) with varying alkoxy chains to control molecular packing modes.[182] Sulfone is a well-known electron acceptor unit for constructing organic emitters with TADF or RTP properties. This is primarily due to the n–π* transitions of its nonbonding electrons and the heavy atom effect of the sulfur atom ($Z = 16$), which enhances SOC. All the resulting molecules exhibited nearly identical PL properties, along with significant TADF and minimal reabsorption features in both dilute solutions and doped films. Among them, C6 demonstrates the highest RL with a maximum LY of 16 558 photons per MeV under X-ray stimulation. Additionally, the rigid and flexible C6-based scintillator screens achieve high X-ray imaging resolutions of 15.0 and 10.6 lp mm^{-1}, respectively.

However, heavy atoms could also lead to emission quenching. Consequently, novel strategies have been developed for the luminescence processes of organic scintillator systems by modifying the interactions between donors and acceptors. High-efficient organic TADF or RTP materials can be achieved by synthesizing supramolecular donor macrocycles and introducing acceptor molecules into the macrocycle's cavity, forming an intermolecular donor–acceptor system. In 2024, Zhang *et al.* synthesized the macrocyclic donor molecule calix[3]acridan (C[3]A), incorporating 1,2-dicyanobenzene (DCB) and 4-bromo-1,2-benzenedicarbonitrile (BrDCB) as guests within the macrocyclic cavities to produce macrocyclic co-crystals, specifically DCB@C[3]A and BrDCB@C[3]A. These co-crystals exhibit green (541 nm, DCB@C[3]A) and orange (633 nm, BrDCB@C[3]A) emissions, respectively (Fig. 7e).[183] This demonstrates that adjusting the electron-donating ability of the macrocycle or the electron-accepting ability of the guest molecules can alter the scintillation color of the co-crystals, offering a simplified method for color tuning compared to covalently bonded scintillators. Furthermore, DCB@C[3]A shows the lowest detection limit of 77.1 nGy s^{-1}. In 2024, Wang *et al.* presented a method for obtaining color-tunable organic scintillator materials, with emission wavelengths ranging from 520 to 682 nm by doping with different guest materials (Fig. 7f), suitable for X-ray imaging through host–guest doping strategy.[184] Yang *et al.* prepared a series of *p*-terphenyl crystals doped with large-sized conjugated molecules (anthracene, tetracene, pentacene, chrysene, and picene) using the thermal field-elevating Bridgman method, resulting in tunable luminescence ranging from 360 to 680 nm under X-ray radiation.[185]

In addition to the methods mentioned above, some purely organic materials have been selected as scintillators due to their inherent properties. In 2024, Chen *et al.* extended the applications of rylene diimides to X-ray imaging, demonstrating superior scintillation properties with reduced non-radiative transitions.[186] This improvement is attributed to the increased π–π plane distances, extended slip distances, and reduced π-plane overlap. The organic scintillator exhibits a low detection limit of 70.68 nGy s^{-1} and a short decay time of 4.37 ns,

while achieving a high spatial resolution of 11.0 lp mm^{-1}. Additionally, Zhang *et al.* demonstrated that the oxidized 1,8-naphthalimide-phenothiazine dyad (OMNI-PTZ 2) with HLCT-excited states showed an enhanced overlap integral between the highest occupied molecular orbital (HOMO) and the lowest unoccupied molecular orbital (LUMO) on MNI π-orbitals, as well as moderate donor–acceptor electron interactions.[187] Consequently, OMNI-PTZ 2(G) exhibits significantly increased RL and greatly reduced decay lifetime, achieving an X-ray dose sensitivity of 97 nGy s^{-1} and an exceptional spatial resolution of 20 lp mm^{-1} (Fig. 7g). Furthermore, Du *et al.* developed a new family of hot exciton scintillators, which were characterized by a large energy gap between the high-lying and lowest triplet states and a small energy difference between triplet and singlet states.[188] 1,1,2,2-Tetrakis(4-bromophenyl) ethylene demonstrates an ultrafast radiative lifetime of 1.79 ns and a LY of approximately 34 600 photons per MeV, showing an excellent combination of high LY and short decay time.

Organic materials, leveraging their structural diversity and tunability, have been extensively investigated for scintillation applications. However, reports on purely organic molecular scintillators remain relatively scarce compared to inorganic or hybrid organic–inorganic systems. This disparity stems from intrinsic limitations: spin-forbidden transitions impose fundamental constraints on LY optimization through molecular design alone, while their inherently low Z_{eff} further limits their efficacy in high-energy radiation absorption.[189]

3.6 Specialized structure scintillators

The previously discussed advancements in scintillators focus on innovative, high-performance compounds with the goal of synthesizing even more superior scintillators. Furthermore, unique structures have been incorporated into the design of scintillator materials to enhance their performance.[190–192] In this regard, Lin *et al.* proposed the concept of 'structural engineering', which, through internal or external design at scales ranging from micro to macro, offered a promising strategy that not only enhanced the performance of scintillators but also broadened their functionality in specific applications such as radiation imaging and therapy, opening up new avenues for candidate materials.[193] Likewise, Roques-Carmes *et al.* proposed a first-principles theory of nanophotonic scintillators and demonstrated order-of-magnitude scintillation enhancements in two different platforms.[194] Furthermore, the arraying of scintillators through specialized structures to enhance photon yield or resolution is a common approach. In

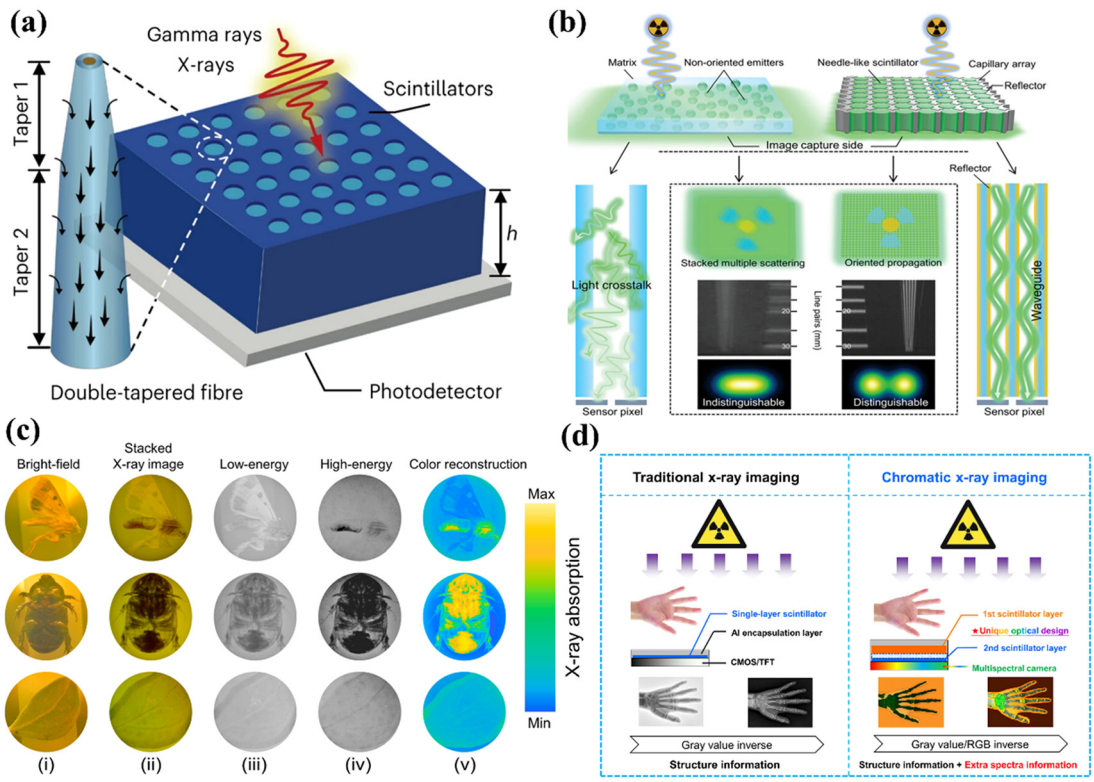

Fig. 8 (a) Schematic representation of scintillator-encapsulated fiber arrays for the detection and imaging of X-rays and gamma rays. Within the fiber array, radioluminescence can propagate over several centimeters. Without the fiber array, however, the radioluminescence becomes attenuated and undetectable due to absorption and scattering within the scintillator layer. (b) Mechanisms of light propagation and the performance of conventional unstructured scintillators *versus* structured capillary needle-like array scintillators in X-ray imaging. (c) Bright-field (i), stacked (ii), decomposed (iii and iv), and color-reconstructed (v) dual-energy X-ray images of a moth, a beetle, and a leaf, utilizing the top–filter–bottom sandwich structure scintillator. (d) Comparison of traditional X-ray imaging approaches and chromatic X-ray imaging strategies.

the design of such structures, three primary objectives are typically pursued: the growth of high-quality scintillators of appropriate thickness, increasing the refractive index contrast between the scintillator and its matrix, and optimizing the photon structure within the scintillator array.[195] In 2023, Dierks *et al.* reported that they synthesized $CsPbBr_3$ nanowires in anodized aluminum oxide and achieved sufficient stability for X-ray micro-tomography under ambient conditions, as well as high spatial resolution.[196] In the same year, Yi *et al.* proposed the design of double-tapered optical-fiber arrays, which could drastically increase the light-collection efficiency and imaging resolution (Fig. 8a).[197] They achieved a spatial resolution of 22 lp mm^{-1} and pixelated gamma-ray imaging with a thickness of 4 mm and ~10 000 pixels under focused 6 MeV irradiation. Moreover, the dose rate (3.5 nGy s^{-1} to 96 mGy s^{-1}) can be conveniently monitored. Then in 2024, considering that the absence of X-ray energy distinction resulted in insufficient image contrast, Ran *et al.* presented an innovative multi-energy X-ray linear-array detector based on $Cs_3Cu_2I_5$.[105] Benefiting from negligible self-absorption of the material and side-illuminated scintillation scenarios, the incident X-ray spectra could be reconstructed by analyzing the distribution of scintillator intensity while illuminated from the side, and the outcome error could be kept below 5.63%. Subsequently, Shao *et al.* fabricated a thick pixelated needle-like array scintillator capable of micrometer resolution (Fig. 8b).[198] They achieved ultrahigh spatial resolutions of 60.8 lp mm^{-1} (the thickness of the scintillators is 0.5 mm) and 51.7 lp mm^{-1} (the thickness of the scintillators is 1 mm) at a MTF of 0.2 due to isolated light-crosstalk channels and robust light output. More recently, Song *et al.* proposed an anti-scattering $CsPbBr_3$ scintillator array embedded within a polyurethane acrylate matrix, which could suppress light scattering and enhance the light collection efficiency by nearly two times compared to the monolithic film.[199] Due to the large refractive index contrast between the scintillator and matrix, the scintillator array exhibits a low dosage and high resolution.

In addition to the specialized structures mentioned above, dual-energy X-ray imaging (DEXI) is cutting-edge technology that provides more detailed information about specific materials compared to traditional single-energy X-ray imaging strategies. In 2023, Shao *et al.* demonstrated a top–filter–bottom sandwich structure scintillator for high-resolution DEXI within a single exposure, achieving an excellent resolution of approximately 18 lp mm^{-1} on stacked images (Fig. 8c).[200] Subsequently, Hu *et al.* successfully achieved color recognition of objects with different densities by using the scintillators of mutually inactive $(BA)_2PbBr_4$:Mn and $Cs_3Cu_2I_5$:TI, which contributed to the application of color X-ray imaging in real-world scenarios (Fig. 8d).[201]

4. Conclusion and outlook

In conclusion, we first provide a comprehensive overview of the various parameters and performance standards of scintillators to facilitate the assessment of their efficacy in recent studies. In recent years, the field of scintillators has garnered significant attention and experienced rapid development.

Lead-based perovskite scintillators exhibit exceptional potential for X-ray detection due to their tunable optoelectronic properties, high spatial resolution, and rapid responses. However, their practical application is hindered by intrinsic challenges: environmental and health concerns from lead toxicity, structural instability under exposure to moisture and oxygen, and luminescence degradation under operational stress. Recent strategies, such as polymer encapsulation, metal–organic framework confinement, and defect-passivating ligand systems, have improved the stability by suppressing ion migration and environmental degradation. Concurrently, elemental doping and lattice engineering enhance energy transfer efficiency while mitigating self-absorption. On the other hand, lead-free perovskite scintillators, particularly those that are copper-based, double perovskites, and manganese-based halides, have emerged as promising alternatives to their toxic lead-based counterparts, offering a balance of environmental sustainability and high-performance X-ray detection. For instance, copper-based systems, such as $Cs_3Cu_2I_5$ and its derivatives, leverage zero-dimensional structures to localize STEs, suppressing non-radiative recombination while enabling tunable emission and flexible film integration. Innovations in doping, composite engineering, and morphology control further enhance their stability and LYs. Despite these advances, challenges persist, including insufficient carrier mobility in the double perovskites, long-term environmental degradation in certain hybrids, and scalability limitations in synthesis protocols. Future research should prioritize synergistic material designs—combining computational modeling with experimental validation—to engineer defect-tolerant lattices, optimize STE dynamics, and develop hydrophobic interfaces. Scalable fabrication techniques, such as inkjet printing and roll-to-roll processing, must be refined to produce large-area, flexible scintillator films for real-world applications. Additionally, exploring multifunctional systems that integrate radiation detection with stimuli-responsive properties could unlock novel applications in low-dose medical imaging, wearable diagnostics, and industrial nondestructive testing. By bridging material innovation with industrial compatibility, lead-free scintillators are poised to redefine radiation detection technologies, aligning high performance with ecological and operational sustainability.

Copper-based cluster scintillators, particularly those centered on Cu_xI_x architectures, represent a groundbreaking advancement in X-ray detection technologies. These materials harness the unique advantages of STE mechanisms, tunable organic–inorganic hybrid frameworks, and efficient radiative recombination, enabling the development of high-performance, low-toxicity scintillators. By optimizing ligand–core charge transfer states and structural engineering, they achieve near-unity PLQYs, ultralow detection limits, and exceptional spatial resolution, while demonstrating remarkable flexibility and environmental stability. Innovations in green synthesis,

such as ionic liquid solvents and mechanochemical approaches, further promote lead-free, energy-efficient fabrication processes, laying the foundation for scalable applications. Nevertheless, critical challenges persist. Moisture and oxygen sensitivity in certain materials compromise long-term stability and self-absorption effects and intricate synthesis protocols hinder large-scale production. Future research is expected to prioritize multifunctional solutions: enhancing stability through hydrophobic ligand design, glass-ceramic encapsulation, or MOF-based confinement; leveraging high-throughput computational models to refine STE energy levels and carrier transport dynamics; and advancing scalable manufacturing techniques like inkjet printing and roll-to-roll processing to bridge laboratory innovations with industrial deployment. Furthermore, it is necessary to increase the solubility of materials to reduce the scattering problem of scintillator films. The transformative potential of copper-based nanoclusters lies in their synergistic integration of performance, flexibility and sustainability. Their application in low-dose medical imaging, industrial nondestructive testing, and deep-space radiation monitoring holds immense promise.

Rare-earth-doped scintillator materials have garnered considerable attention as next-generation candidates for radiation detection and imaging applications. The introduction of rare-earth ions, acting as efficient luminescence centers, markedly enhances energy transfer efficiency and scintillation yield, owing to their distinctive 4f–5d electronic transitions. This quantum efficiency improvement translates to superior radiation sensitivity and spectral resolution, which are particularly crucial for low-dose radiography and nuclear medicine diagnostics. The incorporation of rare-earth dopants not only improves radiation hardness but also enhances thermal stability through optimized lattice interactions, ensuring operational reliability in extreme environments ranging from cryogenic detectors to aerospace systems. Furthermore, the engineered energy level configurations of rare-earth ions enable tunable emission spectra spanning near-UV to near-IR wavelengths, facilitating spectral matching with various photodetectors. It is recommended to strengthen mechanistic investigations into multivalent rare-earth activator configurations to elucidate quantitative structure–property relationships between complex energy level structures and optoelectronic characteristics, thereby formulating design principles for targeted applications including medical imaging and particle physics instrumentation. Moreover, exploring longer fluorescence lifetime modulation techniques expands innovative implementations in emerging optoelectronics such as temporal information encryption and anti-counterfeiting. A multidisciplinary approach integrating multiscale simulations with advanced characterization methodologies should be prioritized to overcome current limitations in understanding structure–performance correlations of rare-earth scintillators. It is crucial to emphasize that research on lanthanum-doped scintillator materials requires the systematic reporting of comprehensive performance metrics. The prevalent practice of overemphasizing isolated parameters while neglecting other critical performance indicators constitutes a detrimental research tendency that could impede the healthy development of this field.

Organic scintillators have undergone transformative advancements through strategic manipulation of excited-state dynamics and molecular architectures, positioning them as viable alternatives to conventional inorganic systems. Recent breakthroughs in TADF and RTP materials have effectively addressed the intrinsic limitations of triplet exciton utilization in organic systems. Some innovations, such as introducing heavy-atom effects to amplify spin–orbit coupling, achieve record-breaking LYs while enabling tunable emission mechanisms between TADF and phosphorescence. Despite these achievements, critical challenges persist, including radiation-induced degradation, oxygen quenching of triplet states, and scalability limitations arising from batch-to-batch performance variations. Looking ahead, the field must prioritize the development of hybrid organic–inorganic architectures to reconcile the low-*Z* limitations of organic matrices with the high stopping power of embedded heavy-element nanostructures. Furthermore, engineering environmentally robust systems, such as oxygen-insensitive RTP scintillators *via* steric encapsulation or crosslinked polymer networks, will be essential for real-world deployment in medical imaging and aerospace environments. To bridge the gap between laboratory innovation and industrial adoption, concerted efforts must focus on establishing standardized benchmarking protocols and elucidating universal structure–property relationships governing triplet harvesting efficiency. Success in these endeavors could redefine performance paradigms across radiation detection technologies, ultimately enabling organic scintillators to transcend niche applications and compete at the forefront of high-energy physics, next-generation radiography, and portable radiation monitoring systems.

Beyond the development of high-performance scintillators, employing specialized structures to enhance the performance of scintillators has also emerged as a highly viable solution. The integration of scintillator materials with matrix materials featuring unique structures can significantly elevate the LY, stability, and detection resolution of the scintillators. This approach further enhances the potential of scintillators for practical applications. Moreover, DEXI offers a remarkably innovative and promising direction for the advancement of X-ray detection. This design provides the possibility of color recognition between objects of varying densities, thereby promoting the advancement of chromatic X-ray imaging in practical applications. However, studies on the impact of structural factors on optical performance have not been sufficiently developed. Future studies should prioritize the exploration of innovative optical architectures in X-ray scintillator systems, with particular emphasis on harnessing micro–nano-structural engineering to enhance photonic characteristics, thereby advancing scintillation performance and diversifying potential applications across radiation detection domains.

In summary, the shared purposes are to develop scintillators with flexibility, high LY, excellent stability, and high

resolution. We aspire for this review to enhance researchers' understanding of the overall progress in scintillator development, serving as a foundation for the creation of materials with superior performance, and more importantly, offering recommendations for future research directions. The primary purpose of this review is to revisit and update recent advancements in scintillators, while offering reliable recommendations for future developments in this field.

Data availability

No primary research results, software or code have been included and no new data were generated or analysed as part of this review.

Conflicts of interest

There are no conflicts to declare.

Acknowledgements

This research was funded by the National Natural Science Foundation of China (No. 62274024), the Natural Science Foundation Program of Sichuan Province (No. 2024NSFSC0232), a Key Teacher Start-Up Research Grant from UESTC (No. Y030202059018069) and the Xiaomi Young Scholars Fellowship.

References

1 P. Büchele, M. Richter, S. F. Tedde, G. J. Matt, G. N. Ankah, R. Fischer, M. Biele, W. Metzger, S. Lilliu, O. Bikondoa, J. E. Macdonald, C. J. Brabec, T. Kraus, U. Lemmer and O. Schmidt, X-ray imaging with scintillator-sensitized hybrid organic photodetectors, *Nat. Photonics*, 2015, **9**, 843–848.
2 X. Xu, W. Qian, S. Xiao, J. Wang, S. Zheng and S. Yang, Halide perovskites: A dark horse for direct X–ray imaging, *EcoMat*, 2020, **2**, e12064.
3 M. J. Yaffe and J. A. Rowlands, X-ray detectors for digital radiography, *Phys. Med. Biol.*, 1997, **42**, 1–39.
4 B. G. M. Durie and S. E. Salmon, High Speed Scintillation Autoradiography, *Science*, 1976, **190**, 1093–1095.
5 P. Lecoq, Development of new scintillators for medical applications, *Nucl. Instrum. Methods Phys. Res., Sect. A*, 2016, **809**, 130–139.
6 W. C. Röntgen, On a New Kind of Rays, *Science*, 1896, **3**, 227–231.
7 Q. Ma, Y. Cao, X. Ge, Z. Zhang, S. Gao and J. Song, X–Ray Excited Luminescence Materials for Cancer Diagnosis and Theranostics, *Laser Photonics Rev.*, 2023, **18**, 2300565.
8 Z. Hong, Z. Chen, Q. Chen and H. Yang, Advancing X-ray Luminescence for Imaging, Biosensing, and Theragnostics, *Acc. Chem. Res.*, 2022, **56**, 37–51.
9 H. Hu, G. Niu, Z. Zheng, L. Xu, L. Liu and J. Tang, Perovskite semiconductors for ionizing radiation detection, *EcoMat*, 2022, **4**, e12258.
10 M. Nikl and A. Yoshikawa, Recent R&D Trends in Inorganic Single–Crystal Scintillator Materials for Radiation Detection, *Adv. Opt. Mater.*, 2015, **3**, 463–481.
11 J. D. Valentine, D. K. Wehe, G. F. Knoll and C. E. Moss, Temperature dependence of CsI (T1) absolute scintillation yield, *IEEE Trans. Nucl. Sci.*, 1993, **40**, 1267–1274.
12 W. Mengesha, T. D. Taulbee, B. D. Rooney and J. D. Valentine, Light yield nonproportionality of CsI(Tl), CsI(Na), and YAP, *IEEE Trans. Nucl. Sci.*, 1998, **45**, 456–461.
13 H. Grassmann, E. Lorenz and H.-G. Moser, Properties of CsI(TI)—Renaissance of an old scintillation material, *Nucl. Instrum. Methods Phys. Res., Sect. A*, 1985, **228**, 323–326.
14 M. K. a, J. P. b and M. Moszyński, Comparison of YAP and BGO for high-resolution PET detectors, *Nucl. Instrum. Methods Phys. Res., Sect. A*, 1998, **404**, 413–417.
15 M. J. Weber and R. R. Monchamp, Luminescence of Bi4Ge3O12: Spectral and decay properties, *J. Appl. Phys.*, 1973, **44**, 5495–5499.
16 Y. Zhou, J. Chen, O. M. Bakr and O. F. Mohammed, Metal Halide Perovskites for X-ray Imaging Scintillators and Detectors, *ACS Energy Lett.*, 2021, **6**, 739–768.
17 C. Dujardin, E. Auffray, E. Bourret-Courchesne, P. Dorenbos, P. Lecoq, M. Nikl, A. N. Vasil'ev, A. Yoshikawa and R. Y. Zhu, Needs, Trends, and Advances in Inorganic Scintillators, *IEEE Trans. Nucl. Sci.*, 2018, **65**, 1977–1997.
18 B. K. Cha, J. Y. Kim, T. J. Kim, C. Sim and G. Cho, Fabrication and imaging characterization of high sensitive CsI(Tl) and Gd_2O2S(Tb) scintillator screens for X-ray imaging detectors, *Radiat. Meas.*, 2010, **45**, 742–745.
19 M. Laval, M. Moszyński, R. Allemand, E. Cormoreche, P. Guinet, R. Odru and J. Vacher, Barium fluoride—Inorganic scintillator for subnanosecond timing, *Nucl. Instrum. Methods Phys. Res.*, 1983, **206**, 169–176.
20 C. D. Brandle, Czochralski growth of oxides, *J. Cryst. Growth*, 2004, **264**, 593–604.
21 L. Qin, H. Li, S. Lu, D. Ding and G. Ren, Growth and characteristics of LYSO (Lu2(1−x−y)Y2xSiO5:Cey) scintillation crystals, *J. Cryst. Growth*, 2005, **281**, 518–524.
22 M. J. Weber, Inorganic scintillators: today and tomorrow, *J. Lumin.*, 2002, **100**, 35–45.
23 F. Maddalena, L. Tjahjana, A. Xie, Arramel, S. Zeng, H. Wang, P. Coquet, W. Drozdowski, C. Dujardin, C. Dang and M. D. Birowosuto, Inorganic, Organic, and Perovskite Halides with Nanotechnology for High–Light Yield X- and γ-ray Scintillators, *Crystals*, 2019, **9**, 88.
24 Q. Chen, J. Wu, X. Ou, B. Huang, J. Almutlaq, A. A. Zhumekenov, X. Guan, S. Han, L. Liang, Z. Yi, J. Li,

X. Xie, Y. Wang, Y. Li, D. Fan, D. B. L. Teh, A. H. All, O. F. Mohammed, O. M. Bakr, T. Wu, M. Bettinelli, H. Yang, W. Huang and X. Liu, All-inorganic perovskite nanocrystal scintillators, *Nature*, 2018, **561**, 88–93.

25 Y. Wang, M. Li, Z. Chai, Y. Wang and S. Wang, Perovskite Scintillators for Improved X–ray Detection and Imaging, *Angew. Chem., Int. Ed.*, 2023, **62**, e202304638.

26 Q. Zhou, W. Li, J. Xiao, A. Li and X. Han, Low–Dimensional Metal Halide for High Performance Scintillators, *Adv. Funct. Mater.*, 2024, **34**, 2402902.

27 J. Fan, H. Li, W. Liu and G. Ouyang, Fabrication Strategies of Mn2+-Based Scintillation Screens for X-Ray Detection and Imaging, *Angew. Chem., Int. Ed.*, 2025, **64**, e202425661.

28 W. Zhao, X. Huang, S. Hu, F. Yang and J. Zhong, Rare-earth nanocrystalline scintillators for biomedical application: A review, *Ceram. Int.*, 2024, DOI: **10.1016/j.ceramint.2024.08.149**.

29 C. Xie, P. You, Z. Liu, L. Li and F. Yan, Ultrasensitive broadband phototransistors based on perovskite/organic-semiconductor vertical heterojunctions, *Light: Sci. Appl.*, 2017, **6**, e17023–e17023.

30 F. Zhou, Z. Li, W. Lan, Q. Wang, L. Ding and Z. Jin, Halide Perovskite, a Potential Scintillator for X-Ray Detection, *Small Methods*, 2020, **4**, 2000506.

31 J. H. Heo, D. H. Shin, J. K. Park, D. H. Kim, S. J. Lee and S. H. Im, High-Performance Next-Generation Perovskite Nanocrystal Scintillator for Nondestructive X-Ray Imaging, *Adv. Mater.*, 2018, **30**, 1801743.

32 D. Rutstrom, L. Stand, M. Koschan, C. L. Melcher and M. Zhuravleva, Europium concentration effects on the scintillation properties of Cs4SrI6:Eu and Cs4CaI6:Eu single crystals for use in gamma spectroscopy, *J. Lumin.*, 2019, **216**, 116740.

33 Y. Zhang, R. Sun, X. Ou, K. Fu, Q. Chen, Y. Ding, L.-J. Xu, L. Liu, Y. Han, A. V. Malko, X. Liu, H. Yang, O. M. Bakr, H. Liu and O. F. Mohammed, Metal Halide Perovskite Nanosheet for X-ray High-Resolution Scintillation Imaging Screens, *ACS Nano*, 2019, **13**, 2520–2525.

34 A. Shinde, R. Gahlaut and S. Mahamuni, Low-Temperature Photoluminescence Studies of CsPbBr 3 Quantum Dots, *J. Phys. Chem. C*, 2017, **121**, 14872–14878.

35 S. M. Ferro, M. Wobben and B. Ehrler, Rare-earth quantum cutting in metal halide perovskites – a review, *Mater. Horiz.*, 2021, **8**, 1072–1083.

36 T. Cai, J. Wang, W. Li, K. Hills-Kimball, H. Yang, Y. Nagaoka, Y. Yuan, R. Zia and O. Chen, Mn(2+)/Yb(3+) Codoped CsPbCl(3) Perovskite Nanocrystals with Triple-Wavelength Emission for Luminescent Solar Concentrators, *Adv. Sci.*, 2020, **7**, 2001317.

37 L. Zi, J. Song, N. Wang, T. Wang, W. Li, H. Zhu, W. Xu and H. Song, X–Ray Quantum Cutting Scintillator Based on CsPbClx,Br3−x:Yb3+ Single Crystals, *Laser Photonics Rev.*, 2023, **17**, 2200852.

38 X. Wu, Z. Guo, S. Zhu, B. Zhang, S. Guo, X. Dong, L. Mei, R. Liu, C. Su and Z. Gu, Ultrathin, Transparent, and High Density Perovskite Scintillator Film for High Resolution X–Ray Microscopic Imaging, *Adv. Sci.*, 2022, **9**, 2200831.

39 S. Chen, W. Liu, M. Xu, P. Shi and M. Zhu, Electrospray prepared flexible CsPbBr 3 perovskite film for efficient X-ray detection, *J. Mater. Chem. C*, 2023, **11**, 8431–8437.

40 A. Erroi, F. Carulli, F. Cova, I. Frank, M. L. Zaffalon, J. Llusar, S. Mecca, A. Cemmi, I. Di Sarcina, F. Rossi, L. Beverina, F. Meinardi, I. Infante, E. Auffray and S. Brovelli, Ultrafast Nanocomposite Scintillators Based on Cd-Enhanced CsPbCl 3 Nanocrystals in Polymer Matrix, *ACS Energy Lett.*, 2024, **9**, 2333–2342.

41 B. Zhang, G. Lyu, E. A. Kelly and R. C. Evans, Forster Resonance Energy Transfer in Luminescent Solar Concentrators, *Adv. Sci.*, 2022, **9**, e2201160.

42 H. Dierks, Z. Zhang, N. Lamers and J. Wallentin, 3D X-ray microscopy with a $CsPbBr_3$ nanowire scintillator, *Nano Res.*, 2023, **16**, 1084–1089.

43 N. Z. Galunov, I. F. Khromiuk and O. A. Tarasenko, Features of pulse shape discrimination capability of organic heterogeneous scintillators, *Nucl. Instrum. Methods Phys. Res., Sect. A*, 2020, **949**, 162870.

44 K. Kagami, M. Koshimizu, Y. Fujimoto, S. Kishimoto, R. Haruki, F. Nishikido and K. Asai, High-energy X-ray detection capabilities of Hf-loaded plastic scintillators synthesized by sol–gel method, *J. Mater. Sci.: Mater. Electron.*, 2020, **31**, 896–902.

45 F. Cao, X. Xu, D. Yu and H. Zeng, Lead-free halide perovskite photodetectors spanning from near-infrared to X-ray range: a review, *Nanophotonics*, 2021, **10**, 2221–2247.

46 G. C. Papavassiliou, Optical properties of small inorganic and organic metal particles, *Prog. Solid State Chem.*, 1979, **12**, 185–271.

47 M. D. Birowosuto, D. Cortecchia, W. Drozdowski, K. Brylew, W. Lachmanski, A. Bruno and C. Soci, X-ray Scintillation in Lead Halide Perovskite Crystals, *Sci. Rep.*, 2016, **6**, 37254.

48 P. Y. D. Maulida, S. Hartati, D. Kowal, L. J. Diguna, M. A. Kuddus Sheikh, M. H. Mahyuddin, I. Mulyani, D. Onggo, F. Maddalena, A. Bachiri, M. E. Witkowski, M. Makowski, W. Drozdowski, Arramel and M. D. Birowosuto, Organic Chain Length Effect on Trap States of Lead Halide Perovskite Scintillators, *ACS Appl. Energy Mater.*, 2023, **6**, 5912–5922.

49 H. Chen, M. Lin, Y. Zhu, D. Zhang, J. Chen, Q. Wei, S. Yuan, Y. Liao, F. Chen, Y. Chen, M. Lin and X. Fang, Halogen–bonding boosting the high performance X–ray imaging of organic scintillators, *Small*, 2024, **20**, 2307277.

50 D. Yu, P. Wang, F. Cao, Y. Gu, J. Liu, Z. Han, B. Huang, Y. Zou, X. Xu and H. Zeng, Two-dimensional halide perovskite as β-ray scintillator for nuclear radiation monitoring, *Nat. Commun.*, 2020, **11**, 3395.

51 W. Shao, X. Wang, Z. Zhang, J. Huang, Z. Han, S. Pi, Q. Xu, X. Zhang, X. Xia and H. Liang, Highly Efficient and Flexible Scintillation Screen Based on Manganese(II) Activated 2D Perovskite for Planar and Nonplanar High–Resolution X–Ray Imaging, *Adv. Opt. Mater.*, 2022, **10**, 2102282.

52 M. Xia, Z. Xie, H. Wang, T. Jin, L. Liu, J. Kang, Z. Sang, X. Yan, B. Wu, H. Hu, J. Tang and G. Niu, Sub–Nanosecond 2D Perovskite Scintillators by Dielectric Engineering, *Adv. Mater.*, 2023, **35**, 2211769.
53 E. Mosconi, J. M. Azpiroz and F. De Angelis, Ab Initio Molecular Dynamics Simulations of Methylammonium Lead Iodide Perovskite Degradation by Water, *Chem. Mater.*, 2015, **27**, 4885–4892.
54 A. Jana, S. Cho, S. A. Patil, A. Meena, Y. Jo, V. G. Sree, Y. Park, H. Kim, H. Im and R. A. Taylor, Perovskite: Scintillators, direct detectors, and X-ray imagers, *Mater. Today*, 2022, **55**, 110–136.
55 F. Cao, D. Yu, W. Ma, X. Xu, B. Cai, Y. M. Yang, S. Liu, L. He, Y. Ke, S. Lan, K.-L. Choy and H. Zeng, Shining Emitter in a Stable Host: Design of Halide Perovskite Scintillators for X-ray Imaging from Commercial Concept, *ACS Nano*, 2020, **14**, 5183–5193.
56 B. Wang, J. Peng, X. Yang, W. Cai, H. Xiao, S. Zhao, Q. Lin and Z. Zang, Template Assembled Large–Size CsPbBr 3 Nanocomposite Films toward Flexible, Stable, and High–Performance X–Ray Scintillators, *Laser Photonics Rev.*, 2022, **16**, 2100736.
57 H. Lv, Q. Hao, N. Yan, L. Ma and M. Chen, Large-area in situ growth of a flexible perovskite scintillator film for X-ray indirect detection applications, *J. Mater. Chem. C*, 2024, **12**, 8970–8976.
58 W. Zheng, H. Zhang, X. Wang, X. Zhang, T. Long, H. Wang, W. W. Yu and C. Zhou, Dual Function Polymer Ligands of Perovskite Nanocrystals for Extraordinary Water Resistance and X–Ray Imaging Scintillators, *Adv. Opt. Mater.*, 2023, **12**, 2301241.
59 J. Shen, R. Jia, Y. Hu, W. Zhu, K. Yang, M. Li, D. Zhao, J. Shi and J. Lian, Cold-Sintered All-Inorganic Perovskite Bulk Composite Scintillators for Efficient X-ray Imaging, *ACS Appl. Mater. Interfaces*, 2024, **16**, 24703–24711.
60 J. Chen, G. Jiang, E. Hamann, H. Mescher, Q. Jin, I. Allegro, P. Brenner, Z. Li, N. Gaponik, A. Eychmuller and U. Lemmer, Organosilicon-Based Ligand Design for High-Performance Perovskite Nanocrystal Films for Color Conversion and X-ray Imaging, *ACS Nano*, 2024, **18**, 10054–10062.
61 H. Wu, P. Ran, L. Yao, H. Cai, W. Cao, Y. Cui, Y. Michael Yang, D. Yang and G. Qian, Confinement of methylammonium lead bromide nanocrystals in metal–organic frameworks as a stable scintillator for high-performance X-ray imaging, *Chem. Eng. J.*, 2024, **491**, 152098.
62 R. Li, W. Zhu, H. Wang, Y. Jiao, Y. Gao, R. Gao, R. Wang, H. Chao, A. Yu and X. Liu, Ultrastable and flexible glass–-ceramic scintillation films with reduced light scattering for efficient X–ray imaging, *npj Flexible Electron.*, 2024, **8**, 31.
63 Z. Xiang, H. Cao, Y. Wei, W. Wang and X. Ouyang, Bivalent metal ion co-doped methylammonium lead tribromide perovskite nanocrystal scintillator for X-ray imaging, *Chem. Eng. J.*, 2024, **495**, 153432.
64 J. Qiu, H. Zhao, Z. Mu, J. Chen, H. Gu, C. Gu, G. Xing, X. Qin and X. Liu, Turning Nonemissive CsPb2Br5 Crystals into High-Performance Scintillators through Alkali Metal Doping, *Nano Lett.*, 2024, **24**, 2503–2510.
65 R. Subagyo, M. Eid, N. Safitri, R. Hanifah, A. A. Afkauni, L. Zhang, M. Makowski, M. A. K. Sheikh, M. H. Mahyuddin, D. Kowal, M. Witkowski, W. Drozdowski, M. D. Birowosuto, A. Arramel and Y. Kusumawati, Liquid-based cationic ligand engineering in one-dimensional bismuth bromide perovskites: A-site influence on scintillation properties, *J. Mater. Chem. C*, 2025, DOI: **10.1039/D4TC04390A**.
66 J. A. Lai, P. Wang, B. Zheng, T. Xuan, D. Wu, Z. Wang, Y. Wang, W. Zhang, J. Du, P. He, K. An and X. Tang, Enhanced Performance in Cesium Tellurium Chlorine by Hafnium Alloying for X–Ray Computed Tomography Imaging, *Adv. Opt. Mater.*, 2024, **12**, 2303297.
67 F. Zhang, Y. Zhou, Z. Chen, X. Niu, H. Wang, M. Jia, J. Xiao, X. Chen, D. Wu, X. Li, Z. Shi and C. Shan, Large–Area X–Ray Scintillator Screen Based on Cesium Hafnium Chloride Microcrystals Films with High Sensitivity and Stability, *Laser Photonics Rev.*, 2023, **17**, 2200848.
68 W. Ke and M. G. Kanatzidis, Prospects for low-toxicity lead-free perovskite solar cells, *Nat. Commun.*, 2019, **10**, 965.
69 T. Cai, W. Shi, S. Hwang, K. Kobbekaduwa, Y. Nagaoka, H. Yang, K. Hills-Kimball, H. Zhu, J. Wang, Z. Wang, Y. Liu, D. Su, J. Gao and O. Chen, Lead-Free Cs(4)CuSb(2) Cl(12) Layered Double Perovskite Nanocrystals, *J. Am. Chem. Soc.*, 2020, **142**, 11927–11936.
70 M. H. Miah, M. U. Khandaker, M. Aminul Islam, M. Nur-E-Alam, H. Osman and M. H. Ullah, Perovskite materials in X-ray detection and imaging: recent progress, challenges, and future prospects, *RSC Adv.*, 2024, **14**, 6656–6698.
71 H. Tang, Y. Xu, X. Hu, Q. Hu, T. Chen, W. Jiang, L. Wang and W. Jiang, Lead-Free Halide Double Perovskite Nanocrystals for Light-Emitting Applications: Strategies for Boosting Efficiency and Stability, *Adv. Sci.*, 2021, **8**, 2004118.
72 J. C. Dahl, W. T. Osowiecki, Y. Cai, J. K. Swabeck, Y. Bekenstein, M. Asta, E. M. Chan and A. P. Alivisatos, Probing the Stability and Band Gaps of Cs2AgInCl6 and Cs2AgSbCl6 Lead-Free Double Perovskite Nanocrystals, *Chem. Mater.*, 2019, **31**, 3134–3143.
73 S. Ghosh, H. Shankar and P. Kar, Recent developments of lead-free halide double perovskites: a new superstar in the optoelectronic field, *Mater. Adv.*, 2022, **3**, 3742–3765.
74 N. Varnakavi, R. Rajavaram, K. Gupta, P. R. Cha and N. Lee, Scintillation Performance of Mn(II)–Doped Cs2NaBiCl6 Double Perovskite Nanocrystals for X–Ray Imaging Applications, *Adv. Opt. Mater.*, 2024, **12**, 2301868.
75 N. J. Cherepy, R. D. Sanner, P. R. Beck, E. L. Swanberg, T. M. Tillotson, S. A. Payne and C. R. Hurlbut, Bismuth- and lithium-loaded plastic scintillators for gamma and neutron detection, *Nucl. Instrum. Methods Phys. Res., Sect. A*, 2015, **778**, 126–132.
76 H. Chen, Q. Han, H. Qin, Y. Shen, H. Lv, Y. Liu, L. Du, Y. Wang, Y. He and W. Ning, Highly stable bismuth-chlor-

ide perovskite X-ray direct detectors with an ultralow detection limit, *Chem. Sci.*, 2025, **16**, 4768–4774.
77 J. Li, Q. Hu, J. Xiao and Z. G. Yan, High-stability double perovskite scintillator for flexible X-ray imaging, *J. Colloid Interface Sci.*, 2024, **671**, 725–731.
78 V. Naresh, P.-R. Cha and N. Lee, Cs2NaGdCl6:Tb3+–A Highly Luminescent Rare-Earth Double Perovskite Scintillator for Low-Dose X-ray Detection and Imaging, *ACS Appl. Mater. Interfaces*, 2024, **16**, 19068–19080.
79 M. Wang, X. Qing, T. Du, C. Wu and X. Han, Te4+-doped Cs2SnCl6 scintillator for flexible and efficient X-ray imaging screens, *J. Mater. Chem. C*, 2024, **12**, 2241–2246.
80 A. Datta, J. Fiala and S. Motakef, 2D perovskite-based high spatial resolution X-ray detectors, *Sci. Rep.*, 2021, **11**, 22897.
81 C.-F. Wang, C.-L. Fang, Y. Feng, S.-Y. Liu, Y. Zhang, H.-Y. Ye, L.-P. Miao and L. Liu, One-dimensional lead-free perovskite single crystals with high X-ray response grown by liquid phase diffusion, *J. Mater. Chem. C*, 2023, **11**, 134–140.
82 M. Zhou, H. Jiang, T. Hou, S. Hou, J. Li, X. Chen, C. Di, J. Xiao, H. Li and D. Ju, Inch-size and thickness-adjustable hybrid manganese halide single-crystalline films for high resolution X-ray imaging, *Chem. Eng. J.*, 2024, **490**, 151823.
83 L. Liu, H. Hu, W. Pan, H. Gao, J. Song, X. Feng, W. Qu, W. Wei, B. Yang and H. Wei, Robust Organogel Scintillator for Self-healing and Ultra-flexible X-ray Imaging, *Adv. Mater.*, 2024, **36**, e2311206.
84 S. Wang, H. Chen, Y. Xu, G. Peng, H. Wang, Q. Li, X. Zhou, Z. Li, Q. Wang and Z. Jin, Organic Cation Modulation in Manganese Halides to Optimize Crystallization Process and X-Ray Response Toward Large-Area Scintillator Screen, *Small*, 2024, e2403234, DOI: **10.1002/smll.202403234**.
85 W. Zhang, P. Sui, W. Zheng, L. Li, S. Wang, P. Huang, W. Zhang, Q. Zhang, Y. Yu and X. Chen, Pseudo-2D Layered Organic-Inorganic Manganese Bromide with a Near-Unity Photoluminescence Quantum Yield for White Light-Emitting Diode and X-Ray Scintillator, *Angew. Chem., Int. Ed.*, 2023, **62**, e202309230.
86 S. B. Xiao, X. Zhang, X. Mao, H. J. Yang, Z. N. Chen and L. J. Xu, Ultrahigh X–Ray Imaging Spatial Resolution Enabled by an 0D Mn(II) Hybrid Scintillator, *Adv. Funct. Mater.*, 2024, **34**, 2404003.
87 J. Zhang, X. Wang, W. Q. Wang, X. Deng, C. Y. Yue, X. W. Lei and Z. Gong, Near-Unity Green Luminescent Hybrid Manganese Halides as X-ray Scintillators, *Inorg. Chem.*, 2024, **63**, 2647–2654.
88 W. Li, Y. Li, Y. Wang, Z. Zhou, C. Wang, Y. Sun, J. Sheng, J. Xiao, Q. Wang, S. Kurosawa, M. Buryi, D. John, K. Paurová, M. Nikl, X. OuYang and Y. Wu, Highly Efficient and Flexible Scintillation Screen Based on Organic Mn(II) Halide Hybrids toward Planar and Nonplanar X–Ray Imaging, *Laser Photonics Rev.*, 2023, **18**, 2300860.
89 Z. Gong, J. Zhang, X. Deng, M. P. Ren, W. Q. Wang, Y. J. Wang, H. Cao, L. Wang, Y. C. He and X. W. Lei, Near–unity broadband emissive hybrid manganese bromides as highly–efficient radiation scintillators, *Aggregate*, 2024, **5**, e574.
90 H. Wang, W. Li, K. Wang, H. Yin, X. Mao and R. Zhang, Turning self-trapped exciton emission via Sb3+ doping in zero-dimensional hybrid indium chloride for X-ray scintillation, *J. Lumin.*, 2024, **269**, 120507.
91 H. Huang, Y. Yang, S. Qiao, X. Wu, Z. Chen, Y. Chao, K. Yang, W. Guo, Z. Luo, X. Song, Q. Chen, C. Yang, Y. Yu and Z. Zou, Accommodative Organoammonium Cations in A–Sites of Sb–In Halide Perovskite Derivatives for Tailoring BroadBand Photoluminescence with X–Ray Scintillation and White–Light Emission, *Adv. Funct. Mater.*, 2024, **34**, 2309112.
92 M. Wang, Z. Zhang, J. Lyu, J. Qiu, C. Gu, H. Zhao, T. Wang, Y. Ren, S. W. Yang, G. Qin Xu and X. Liu, Overcoming Thermal Quenching in X-ray Scintillators through Multi-Excited State Switching, *Angew. Chem., Int. Ed.*, 2024, **63**, e202401949.
93 W. F. Wang, M. J. Xie, P. K. Wang, J. Lu, B. Y. Li, M. S. Wang, S. H. Wang, F. K. Zheng and G. C. Guo, Thermally Activated Delayed Fluorescence (TADF)-active Coinage-metal Sulfide Clusters for High-resolution X-ray Imaging, *Angew. Chem., Int. Ed.*, 2024, **63**, e202318026.
94 S. Yuan, G. Zhang, F. Chen, J. Chen, Y. Zhang, Y. Di, Y. Chen, Y. Zhu, M. Lin and H. Chen, Thermally Activated Delayed Fluorescent Ag(I) Complexes for Highly Efficient Scintillation and High–Resolution X–Ray Imaging, *Adv. Funct. Mater.*, 2024, **34**, 2400436.
95 J. O'Neill, J. Ghosh, S. Alghamdi, I. Braddock, C. Crean, R. Dorey, R. Mulholland, S. Richards, M. Wilson, H. Salway, M. Anaya, J. Reiss, D. Wolfe and P. Sellin, Hydrothermal and Mechanosynthesis of Mixed–Cation Double Perovskite Scintillators for Radiation Detection, *Adv. Opt. Mater.*, 2024, **12**, 2301335.
96 C. Wang, Z.-G. Yan, Y. Wang, J. Zhu, C. Peng, Y. Qu, F. Yang, J. Xiao and X. Han, All-Inorganic Ruddlesden–Popper Perovskite Cs2CdCl4:Mn for Low-Dose and Flexible X-ray Imaging, *ACS Mater. Lett.*, 2024, **6**, 1429–1438.
97 Z. Wang, J. Chen, X. Xu, T. Bai, Q. Kong, H. Yin, Y. Yang, W. W. Yu, R. Zhang, X. Liu and K. Han, B(I)-Site Alkali Metal Engineering of Lead-Free Perovskite Nanocrystals for Efficient X-Ray Detection and Imaging, *Adv. Opt. Mater.*, 2024, **12**, 2302617.
98 H. Cui, W. Zhu, Y. Deng, T. Jiang, A. Yu, H. Chen, S. Liu and Q. Zhao, Lead-free organic–inorganic hybrid scintillators for X-ray detection, *Aggregate*, 2024, **5**, e454.
99 L. Lian, M. Zheng, W. Zhang, L. Yin, X. Du, P. Zhang, X. Zhang, J. Gao, D. Zhang, L. Gao, G. Niu, H. Song, R. Chen, X. Lan, J. Tang and J. Zhang, Efficient and Reabsorption–Free Radioluminescence in Cs 3 Cu 2 I 5 Nanocrystals with Self–Trapped Excitons, *Adv. Sci.*, 2020, **7**, 2000195.
100 Q. Yao, J. Li, X. Li, Y. Ma, H. Song, Z. Li, Z. Wang and X. Tao, Achieving a Record Scintillation Performance by

Micro-Doping a Heterovalent Magnetic Ion in Cs3Cu2I5 Single-Crystal, *Adv. Mater.*, 2023, **35**, 2304938.

101 G. Peng, F. Qiu, Z. Li, H. Wang, Q. Li and Z. Jin, Single–Source Evaporated High–Quality Single–Phase Cs3Cu2I5 Scintillator Films for High Performance X–Ray Imaging, *Adv. Funct. Mater.*, 2024, **34**, 2403052.

102 Z. Wang, L. Wang, J. Xie, Y. Yang, Y. Song, G. Xiao, Y. Fu, L. Zhang, Y. Fang, D. Yang and Q. Dong, HCOO(-) Doping-Induced Multiexciton Emissions in Cs(3)Cu(2)I(5) Crystals for Efficient X-Ray Scintillation, *Small*, 2024, **20**, e2309922.

103 I. K. Moon, S. Yoo, J. Choi, H. K. Kim and Y. Kang, Flexible Wood–Based X–Ray Scintillator Film Using Lead–Free Cs3Cu2I5 Perovskite Nanoparticles, *Small Struct.*, 2024, **5**, 2400043.

104 X. Hao, L. Nie, X. Zhu, G. Zeng, C. Liu, Z. Teng, H. Liu, Y. Yue, X. Yu and T. Wang, High-Resolution X-ray Image from Copper-Based Perovskite Hybrid Polymer, *ACS Appl. Mater. Interfaces*, 2024, **16**, 29210–29216.

105 P. Ran, Q. Yao, J. Hui, Y. Su, L. Yang, C. Kuang, X. Liu and Y. Yang, Multi–Energy X–Ray Linear–Array Detector Enabled by the Side–Illuminated Metal Halide Scintillator, *Laser Photonics Rev.*, 2024, **18**, 2300587.

106 W. Xiang, D. Shen, X. Zhang, X. Li, Y. Liu and Y. Zhang, Transparent and Planar Cs(3)Cu(2)Cl(5) Crystals for Micrometer-Resolution X-ray Imaging Screen, *ACS Appl. Mater. Interfaces*, 2024, **16**, 4918–4924.

107 P. Ran, X. Chen, Z. Chen, Y. Su, J. Hui, L. Yang, T. Liu, X. Tang, H. Zhu, X. J. She and Y. Yang, Metal Halide CsCu2I3 Flexible Scintillator with High Photodiode Spectral Compatibility for X–Ray Cone Beam Computed Tomography (CBCT) Imaging, *Laser Photonics Rev.*, 2024, **18**, 2300743.

108 H. Wu, Q. Wang, A. Zhang, G. Niu, M. Nikl, C. Ming, J. Zhu, Z. Zhou, Y.-Y. Sun, G. Nan, G. Ren, Y. Wu and J. Tang, One-dimensional scintillator film with benign grain boundaries for high-resolution and fast X-ray imaging, *Sci. Adv.*, 2023, **9**, eadh1789.

109 A. Zhang, J. Pang, H. Wu, Q. Tan, Z. Zheng, L. Xu, J. Tang and G. Niu, Event-based X-ray imager with ghosting-free scintillator film, *Optica*, 2024, **11**, 606–611.

110 C. Shu, L. Lei, S. Tie, X. Lu, S. Dong, Z. Fan, N. Yang, R. Yuan, J. Zhu and X. Zheng, Strain-Released Cs5Cu3Cl6I2 Scintillators by Rb+ Doping for High-Resolution X-Ray Imaging, *J. Phys. Chem. C*, 2024, **128**, 6106–6113.

111 Y. Hu, J. Jin, K. Han and Z. Xia, Unveiling The Role of Cu+ Doping in Rb2AgBr3 Scintillators toward Enhanced Photoluminescence Quantum Efficiency and Light Yield, *Adv. Opt. Mater.*, 2024, **12**, 2302063.

112 J. Yao, D. Huang, X. Hu, H. Cheng, D. Wang, X. Li, W. Yang and R. Xie, One-Dimensional Copper-Doped Rb(2)AgI(3) with Efficient Sky-Blue Emission as a High-Performance X-ray Scintillator, *ACS Omega*, 2024, **9**, 28969–28977.

113 Q. Wu, X. Zhou, W. Gui, L. Yao, Y. Wang and C. L. Wang, Rb2AgBr3:Cu scintillators for high performance gamma and X-ray detection, *Chem. Eng. J.*, 2025, **507**, 160815.

114 Z. Wang, Y. Wei, C. Liu, Y. Liu and M. Hong, Mn2+-Activated Cs3Cu2I5 Nano-Scintillators for Ultra-High Resolution Flexible X-Ray Imaging, *Laser Photonics Rev.*, 2023, **17**, 2200851.

115 P. Ran, X. Chen, Z. Chen, Y. Su, J. Hui, L. Yang, T. Liu, X. Tang, H. Zhu, X.-J. She and Y. Yang, Metal Halide CsCu2I3 Flexible Scintillator with High Photodiode Spectral Compatibility for X-Ray Cone Beam Computed Tomography (CBCT) Imaging, *Laser Photonics Rev.*, 2024, **18**, 2300743.

116 P. Mao, Y. Tang, B. Wang, D. Fan and Y. Wang, Organic-Inorganic Hybrid Cuprous Halide Scintillators for Flexible X-ray Imaging, *ACS Appl. Mater. Interfaces*, 2022, **14**, 22295–22301.

117 J. Ni, Q. Cao, K. Xiao, K. Gang, S. Liu, X. Liu and Q. Zhao, Colloidal Copper(I) Iodide Cluster-Based Scintillators for High-Resolution X-Ray Imaging, *Laser Photonics Rev.*, 2025, **19**, 2400963.

118 Y. Wang, T. Zhang, W. Zhao, W. Xu, Z. Wu, Y. D. Suh, Y. Zhang, X. Liu and W. Huang, Machine Learning-Guided Discovery of Copper(I)-Iodide Cluster Scintillators for Efficient X-ray Luminescence Imaging, *Angew. Chem.*, 2025, **64**, e202413672.

119 J. A. Lai, C. Li, Z. Wang, L. Guo, Y. Wang, K. An, S. Cao, D. Wu, Z. Liu, Z. Hu, Y. Leng, J. Du, P. He and X. Tang, Photoluminescence-Tunable organic phosphine cuprous halides clusters for X-ray scintillators and white light emitting diodes, *Chem. Eng. J.*, 2024, **494**, 153077.

120 S. Zhao, J. Zhao, S. M. H. Qaid, D. Liang, K. An, W. Cai, Q. Qian and Z. Zang, White emission metal halides for flexible and transparent X-ray scintillators, *Appl. Phys. Rev.*, 2024, **11**, 011408.

121 N. Zhang, L. Qu, S. Dai, G. Xie, C. Han, J. Zhang, R. Huo, H. Hu, Q. Chen, W. Huang and H. Xu, Intramolecular charge transfer enables highly-efficient X-ray luminescence in cluster scintillators, *Nat. Commun.*, 2023, **14**, 2901.

122 Q.-H. Zou, W.-H. Yang, L.-K. Wu, L.-L. Jiang, S.-H. Wang, L. Liu, R.-F. Li, H.-Y. Ye and J.-R. Li, Ionothermal synthesis of a stable three-dimensional [Cu4I4] cluster scintillator with near-unity quantum efficiency and weak thermal quenching, *Inorg. Chem. Front.*, 2025, **12**, 692–700.

123 Q. Zou, W. Yang, L. Wu, L. Jiang, S. Wang, L. Liu, R. Li, H. Ye and J. Li, Ionothermal synthesis of a hybrid cuprous (I) iodide scintillator with efficient cyan emission and high antiwater stability, *Chem. Eng. J.*, 2025, **506**, 159971.

124 H. Wang, J. X. Wang, X. Song, T. He, Y. Zhou, O. Shekhah, L. Gutierrez-Arzaluz, M. Bayindir, M. Eddaoudi, O. M. Bakr and O. F. Mohammed, Copper Organometallic Iodide Arrays for Efficient X-ray Imaging Scintillators, *ACS Cent. Sci.*, 2023, **9**, 668–674.

125 N. Lin, R. C. Wang, S. Y. Zhang, Z. H. Lin, X. Y. Chen, Z. N. Li, X. W. Lei, Y. Y. Wang and C. Y. Yue, 0D Hybrid Cuprous Halide as an Efficient Light Emitter and X–Ray Scintillator, *Laser Photonics Rev.*, 2023, **17**, 2300427.

126 H.-J. Yang, W. Xiang, X. Zhang, J.-Y. Wang, L.-J. Xu and Z.-N. Chen, High spatial resolution X-ray scintillators

based on a 2D copper(I) iodide hybrid, *J. Mater. Chem. C*, 2024, **12**, 438–442.

127 Q. Kong, X. Jiang, Y. Sun, J. Zhu and X. Tao, Yellow-emissive organic copper(I) halide single crystals with [Cu4I4] cubane unit as efficient X-ray scintillators, *Inorg. Chem. Front.*, 2024, **11**, 3028–3035.

128 H. Lv, W. Shao, H. Chen, G. Zhu, Y. Wang, Z. Zhang and H. Liang, Ultra-Broad Emission Copper Halide Scintillator-Based X-Ray Imager, *Adv. Sci.*, 2025, **12**, 2405995.

129 T. He, Y. Zhou, P. Yuan, J. Yin, L. Gutiérrez-Arzaluz, S. Chen, J.-X. Wang, S. Thomas, H. N. Alshareef, O. M. Bakr and O. F. Mohammed, Copper Iodide Inks for High-Resolution X-ray Imaging Screens, *ACS Energy Lett.*, 2023, **8**, 1362–1370.

130 B. Li, J. Jin, X. Liu, M. Yin, X. Zhang, Z. Xia and Y. Xu, Multiphase Transformation in Hybrid Copper(I)-Based Halides Enable Improved X-ray Scintillation and Real-Time Imaging, *ACS Mater. Lett.*, 2024, **6**, 1542–1548.

131 R. Gu, K. Han, J. Jin, H. Zhang and Z. Xia, Surfactant-Assisted Synthesis of Hybrid Copper(I) Halide Nanocrystals for X-ray Scintillation Imaging, *Chem. Mater.*, 2024, **36**, 2963–2970.

132 Q. C. Peng, Y. B. Si, J. W. Yuan, Q. Yang, Z. Y. Gao, Y. Y. Liu, Z. Y. Wang, K. Li, S. Q. Zang and B. Zhong Tang, High Performance Dynamic X-ray Flexible Imaging Realized Using a Copper Iodide Cluster-Based MOF Microcrystal Scintillator, *Angew. Chem., Int. Ed.*, 2023, **62**, e202308194.

133 Y. V. Demyanov, Z. Ma, Z. Jia, M. I. Rakhmanova, G. M. Carignan, I. Y. Bagryanskaya, V. S. Sulyaeva, A. A. Globa, V. K. Brel, L. Meng, H. Meng, Q. Lin, J. Li and A. V. Artemev, Copper(I)–Arsine Clusters with a Near–Unity Phosphorescence Quantum Yield for X–Ray Scintillation and LED Applications, *Adv. Opt. Mater.*, 2024, **12**, 2302904.

134 P. Yuan, T. He, Y. Zhou, J. Yin, H. Zhang, Y. Zhang, X. Yuan, C. Dong, R. Huang, W. Shao, S. Chen, X. Song, R. Zhou, N. Zheng, M. Abulikemu, M. Eddaoudi, M. Bayindir, O. F. Mohammed and O. M. Bakr, Hybrid Thermally Activated Nanocluster Fluorophores for X-ray Scintillators, *ACS Energy Lett.*, 2023, **8**, 5088–5097.

135 Y. C. Chen, S. Q. Yuan, G. Z. Zhang, Y. M. Di, Q. W. Qiu, X. Yang, M. J. Lin, Y. N. Zhu and H. M. Chen, Mechanochemical Synthesis of Cuprous Complexes for X-ray Scintillation and Imaging, *Inorg. Chem.*, 2024, **63**, 3572–3577.

136 Y.-C. Chen, S.-Q. Yuan, G.-Z. Zhang, Y.-M. Di, Q.-W. Qiu, X. Yang, M.-J. Lin, Y.-N. Zhu and H.-M. Chen, Mechanochemical Synthesis of Cuprous Complexes for X-ray Scintillation and Imaging, *Inorg. Chem.*, 2024, **63**, 3572–3577.

137 X. Wu, Z. Guo, S. Zhu, B. Zhang, S. Guo, X. Dong, L. Mei, R. Liu, C. Su and Z. Gu, Ultrathin, Transparent, and High Density Perovskite Scintillator Film for High Resolution X–Ray Microscopic Imaging, *Adv. Sci.*, 2022, **9**, 2200831.

138 C. Wang, J. Xiao, S. Ma, Y. Li and Z. Yan, Efficient Near–Infrared Emitting Halide Scintillators with Mitigating External Light Crosstalk for Portable X–Ray Imaging, *Adv. Funct. Mater.*, 2024, **34**, 2401995.

139 T. Yang, P. Wu, R. Chen, J. Ni, C. Xu, X. Liu, S. Wang and S. Liu, Enhanced luminescence of Tb doping nanoscintillators based on NaLuF4 host matrix for X-ray imaging, *J. Lumin.*, 2024, **269**, 120498.

140 P. Qiao, J. Yang, H. Ma and L. Lei, Tuning scintillation property of CsLu2F7: Pr crystals for X-ray imaging, *Opt. Mater.*, 2024, **148**, 114812.

141 A. Zhang, S. Xu and L. Lei, Strongly reduced hysteresis scintillation luminescence in lanthanide doped fluoride nanoscintillators, *J. Alloys Compd.*, 2023, **952**, 169845.

142 H. Zou, M. Yi, S. Xu and L. Lei, A hollow NaBiF4:Tb nanoscintillator with ultra-weak afterglow for high-resolution X-ray imaging, *Chem. Commun.*, 2023, **59**, 11732–11735.

143 M. Bungla, M. Tyagi, A. K. Ganguli and P. N. Prasad, A NaBiF4:Gd/Tb nanoscintillator for high-resolution X-ray imaging, *J. Mater. Chem. C*, 2024, **12**, 9595–9605.

144 K. Yang, Y. Yang, D. Sun, S. Li, X. Song and H. Yang, Designing highly UV-emitting lanthanide nanoscintillators for in vivo X-ray-activated tumor therapy, *Sci. China Mater.*, 2023, **66**, 4090–4099.

145 Z. Yang, P. Zhang, X. Chen, Z. Hong, J. Gong, X. Ou, Q. Wu, W. Li, X. Wang, L. Xie, Z. Zhang, Z. Yu, X. Qin, J. Tang, H. Zhang, Q. Chen, S. Han and H. Yang, High–Confidentiality X–Ray Imaging Encryption Using Prolonged Imperceptible Radioluminescence Memory Scintillators, *Adv. Mater.*, 2023, **35**, 2309413.

146 T. Yang, L. Guo, H. Wang, X. Xu, P. Wu, N. Zhang, X. Liu, S. Liu and Q. Zhao, Enhanced radioluminescence of NaLuF4:Eu3+ nanoscintillators by terbium sensitization for X-ray imaging, *Inorg. Chem. Front.*, 2023, **10**, 3974–3982.

147 H. Zhang, B. Zhang, C. Cai, K. Zhang, Y. Wang, Y. Wang, Y. Yang, Y. Wu, X. Ba and R. Hoogenboom, Water-dispersible X-ray scintillators enabling coating and blending with polymer materials for multiple applications, *Nat. Commun.*, 2024, **15**, 2055.

148 H. Lu, X. Xu, Y. Li, G. Feng, J. Yang, X. Huang, Q. Luo, S. Wang and S. Wu, Heterovalent Co–Doped LiLuF4 Composite Flexible Films as Persistent Luminescence Scintillator for X–Ray High–Resolution Extension Imaging, *Adv. Opt. Mater.*, 2024, **12**, 2303134.

149 X. Liu, R. Li, X. Xu, Y. Jiang, W. Zhu, Y. Yao, F. Li, X. Tao, S. Liu, W. Huang and Q. Zhao, Lanthanide(III)–Cu4I4 Organic Framework Scintillators Sensitized by Cluster–Based Antenna for High–Resolution X–ray Imaging, *Adv. Mater.*, 2023, **35**, 2206741.

150 H. Li, Y. Li, L. Zhang, E. Hu, D. Zhao, H. Guo and G. Qian, A Thermo–Responsive MOFs for X–Ray Scintillator, *Adv. Mater.*, 2024, **36**, 2405535.

151 J. Jin, K. Han, Y. Wang and Z. Xia, Bandgap Narrowing in Europium(II)-Based Bromide Hybrids toward Improved

X-ray Scintillation and Imaging, *Chem. Mater.*, 2024, **36**, 4813–4820.

152 J. Yang, H. Lu, L. Yang, Y. Yao, Z. Wei, M. Chen, H. Qi, Y. Ren, Y. Wang, J. Qiu and J. Lin, Lanthanide Organic–Inorganic Hybrids for X-ray Scintillation and Imaging, *Inorg. Chem.*, 2024, **63**, 3642–3647.

153 J. Xu, R. Luo, Z. Luo, J. Xu, Z. Mu, H. Bian, S. Y. Chan, B. Y. H. Tan, D. Chi, Z. An, G. Xing, X. Qin, C. Gong, Y. Wu and X. Liu, Ultrabright molecular scintillators enabled by lanthanide-assisted near-unity triplet exciton recycling, *Nat. Photonics*, 2025, **19**, 71–78.

154 P.-K. Wang, W.-F. Wang, B.-Y. Li, R.-X. Qian, Z.-X. Gao, S.-H. Wang, F.-K. Zheng and G.-C. Guo, Highly sensitive terbium-based metal–organic framework scintillators applied in flexible X-ray imaging, *Inorg. Chem. Front.*, 2025, **12**, 1040–1048.

155 L. Li, J. Chen, X. Peng, T. Jiang, L. Lei and H. Guo, High-resolution Tb3+-doped Gd-based oxyfluoride glass scintillators for X-ray imaging, *J. Mater. Chem. C*, 2023, **11**, 11664–11670.

156 J. Guo, L. Li, J. Chen, H. Li and H. Guo, Ce3+-doped oxyfluoride glass scintillator: optimized radioluminescence and application in X-ray imaging, *J. Alloys Compd.*, 2024, **980**, 173670.

157 Z. Sun, X. Huang, J. Yang, S. Wang and S. Wu, Preparation and scintillation properties of Ce3+/Tb3+-co-doped oxyfluoride glass for high-resolution X-ray imaging, *Ceram. Int.*, 2023, **49**, 15500–15506.

158 L. Li, J. Chen, Z. Wen, J. Guo, Q. Wang and H. Guo, X-ray imaging scintillator: Tb3+-doped oxyfluoride aluminosilicate glass, *Ceram. Int.*, 2024, **50**, 757–763.

159 W. Dai, Q. Zhang, G. A. Ashraf, H. Gong, R. Wei, H. Guo and F. Hu, Novel transparent NaLu2F7:Tb3+ glass-ceramics scintillator for highly resolved X-ray imaging, *Ceram. Int.*, 2024, **50**, 21878–21888.

160 Y. Liu, K. Han, S. Zhao, X. Zhou, S. Gao, Y. Wang, Z. Xia and S. Jiang, Ce3+-doped alkaline-earth sulfide nanocrystals for X-ray scintillation imaging screens, *J. Mater. Chem. C*, 2024, **12**, 3221–3227.

161 D. Wang, H. Li, J. Chen, D. Hou, X. Liu, Z. Yu, S. Lv, J. Qiu and S. Zhou, Congruent Glass Composite Scintillator for Efficient High-Energy Ray Detection, *Adv. Mater.*, 2025, **37**, 2412661.

162 Y. Ling, X. Zhao, P. Hao, Y. Song, J. Liu, L. Zhao, Y. Qian and C. Guo, Gd3+-sensitized rare earth fluoride scintillators for High-resolution flexible X-ray imaging, *Chem. Eng. J.*, 2023, **476**, 146790.

163 T. Wang, S. Hu, T. Ji, X. Zhu, G. Zeng, L. Huang, A. N. Yakovlev, J. Qiu, X. Xu and X. Yu, High–Temperature X–Ray Imaging with Transparent Ceramics Scintillators, *Laser Photonics Rev.*, 2024, **18**, 2300892.

164 J. Yang, X. Huang, X. Xu, H. Lu, S. Wang and S. Wu, Layered Chalcogenide Scintillators Enabled by Reversible Hydrous-Induced Phase Transformation for High-Resolution X-ray Imaging, *ACS Appl. Mater. Interfaces*, 2024, **16**, 15050–15058.

165 S. Wang, J. Yang, C. Liu, W. Li, X. Zheng, X. Qiao, X. Sun, S. Qian, J. Han, J. Wu, X. Xu, J. Ren and J. Zhang, KTb3–GdF10 Nano-Glass Composite Scintillator with Excellent Thermal Stability and Record X-Ray Imaging Resolution, *Laser Photonics Rev.*, 2025, **19**, 2401611.

166 H. Li, P. Wang, G. Lin and J. Huang, The role of rare earth elements in biodegradable metals: A review, *Acta Biomater.*, 2021, **129**, 33–42.

167 D. A. Gkika, M. Chalaris and G. Z. Kyzas, Review of Methods for Obtaining Rare Earth Elements from Recycling and Their Impact on the Environment and Human Health, *Processes*, 2024, **12**, 1235.

168 Y.-H. Chen, G.-Z. Zhang, F.-H. Chen, S.-Q. Zhang, X. Fang, H.-M. Chen and M.-J. Lin, Halogen-bonded charge-transfer co-crystal scintillators for high-resolution X-ray imaging, *Chem. Sci.*, 2024, **15**, 7659–7666.

169 T. F. Manny, T. B. Shonde, H. Liu, M. S. Islam, O. J. Olasupo, J. Viera, S. Moslemi, M. Khizr, C. Chung, J. S. R. V. Winfred, L. M. Stand, E. F. Hilinski, J. Schlenoff and B. Ma, Efficient X-Ray Scintillators Based on Facile Solution Processed 0D Organic Manganese Bromide Hybrid Films, *Adv. Funct. Mater.*, 2025, **35**, 2413755.

170 S. He, P. Wan, H. Li, Z. Bao, X. Sui, G. Zheng, H. Yin, J. Pang, T. Jin, S. Yuan, L. Xu, X. Ouyang, Z. Zheng, L. Liu, G. Niu and J. Tang, Hot Exciton-Based Plastic Scintillator Engineered for Efficient Fast Neutron Detection and Imaging, *Adv. Funct. Mater.*, 2025, 2503688.

171 W. Zhao, Z. He and B. Z. Tang, Room-temperature phosphorescence from organic aggregates, *Nat. Rev. Mater.*, 2020, **5**, 869–885.

172 W. Ma, Y. Su, Q. Zhang, C. Deng, L. Pasquali, W. Zhu, Y. Tian, P. Ran, Z. Chen, G. Yang, G. Liang, T. Liu, H. Zhu, P. Huang, H. Zhong, K. Wang, S. Peng, J. Xia, H. Liu, X. Liu and Y. M. Yang, Thermally activated delayed fluorescence (TADF) organic molecules for efficient X-ray scintillation and imaging, *Nat. Mater.*, 2021, **21**, 210–216.

173 X. Wang, H. Shi, H. Ma, W. Ye, L. Song, J. Zan, X. Yao, X. Ou, G. Yang, Z. Zhao, M. Singh, C. Lin, H. Wang, W. Jia, Q. Wang, J. Zhi, C. Dong, X. Jiang, Y. Tang, X. Xie, Y. Yang, J. Wang, Q. Chen, Y. Wang, H. Yang, G. Zhang, Z. An, X. Liu and W. Huang, Organic phosphors with bright triplet excitons for efficient X-ray-excited luminescence, *Nat. Photonics*, 2021, **15**, 187–192.

174 X. Chen, D. Ma, T. Liu, Z. Chen, Z. Yang, J. Zhao, Z. Yang, Y. Zhang and Z. Chi, Hybridized Local and Charge-Transfer Excited-State Fluorophores through the Regulation of the Donor–Acceptor Torsional Angle for Highly Efficient Organic Light-Emitting Diodes, *CCS Chem.*, 2022, **4**, 1284–1294.

175 Y. X. Hu, J. Miao, T. Hua, Z. Huang, Y. Qi, Y. Zou, Y. Qiu, H. Xia, H. Liu, X. Cao and C. Yang, Efficient selenium-integrated TADF OLEDs with reduced roll-off, *Nat. Photonics*, 2022, **16**, 803–810.

176 C. Dong, X. Wang, W. Gong, W. Ma, M. Zhang, J. Li, Y. Zhang, Z. Zhou, Z. Yang, S. Qu, Q. Wang, Z. Zhao, G. Yang, A. Lv, H. Ma, Q. Chen, H. Shi, Y. Yang and Z. An,

Influence of Isomerism on Radioluminescence of Purely Organic Phosphorescence Scintillators, *Angew. Chem., Int. Ed.*, 2021, **60**, 27195–27200.

177 H. Chen, M. Lin, C. Zhao, D. Zhang, Y. Zhang, F. Chen, Y. Chen, X. Fang, Q. Liao, H. Meng and M. Lin, Highly Efficient, Low–Dose, and Ultrafast Carbazole X–Ray Scintillators, *Adv. Opt. Mater.*, 2023, **11**, 2300365.

178 H. Chen, M. Lin, Y. Zhu, D. Zhang, J. Chen, Q. Wei, S. Yuan, Y. Liao, F. Chen, Y. Chen, M. Lin and X. Fang, Halogen–bonding boosting the high performance X–ray imaging of organic scintillators, *Small*, 2024, **20**, 2307277.

179 T. Chen, Y. Xu, A. Ying, C. Yang, Q. Lin and S. Gong, Through–Space Charge–Transfer Organogold(III) Complexes Enable High–Performance X–ray Scintillation and Imaging, *Angew. Chem., Int. Ed.*, 2024, **63**, e202401833.

180 V. W.-W. Yam, S. W.-K. Choi, T.-F. Lai and W.-K. Lee, Syntheses, crystal structures and photophysics of organogold(III) diimine complexes, *J. Chem. Soc., Dalton Trans.*, 1993, 1001–1002.

181 M. Dong, A. Lv, X. Zou, N. Gan, C. Peng, M. Ding, X. Wang, Z. Zhou, H. Chen, H. Ma, L. Gu, Z. An and W. Huang, Polymorphism–Dependent Organic Room Temperature Phosphorescent Scintillation for X–Ray Imaging, *Adv. Mater.*, 2024, **36**, 2310663.

182 L. Zhan, Y. Xu, T. Chen, Y. Tang, C. Zhong, Q. Lin, C. Yang and S. Gong, Organic molecules with dual triplet–harvesting channels enable efficient X–ray scintillation and imaging, *Aggregate*, 2024, **5**, e485.

183 G. Zhang, F. Chen, Y. Di, S. Yuan, Y. Zhang, X. Quan, Y. Chen, H. Chen and M. Lin, Guest–Induced Thermally Activated Delayed Fluorescence Organic Supramolcular Macrocycle Scintillators for High–Resolution X–Ray Imaging, *Adv. Funct. Mater.*, 2024, **34**, 2404123.

184 H. Wang, C. Peng, M. Chen, Y. Xiao, T. Zhang, X. Liu, Q. Chen, T. Yu and W. Huang, Wide–Range Color–Tunable Organic Scintillators for X–Ray Imaging Through Host–Guest Doping, *Angew. Chem., Int. Ed.*, 2024, **63**, e202316190.

185 W. Yang, P. Han, S. Zhu, Z. Cui, Z. Li, S. Wu, W. Xu, Z. Gao, T. Ba, Y. Liang, H. Jiang and W. Hu, Bulk Organic Doped p-Terphenyl Crystals for X-ray Scintillators with Low Detection Limit, Nanoseconds Decay Time, and Tunable Fluorescence, *ACS Appl. Electron. Mater.*, 2024, **6**, 4223–4231.

186 J. Chen, G. Liu, F. Chen, Y. Chen, X. Fang, H. Chen and M.-J. Lin, Binaphthol diimide scintillators for X-ray imaging, *Sci. China Mater.*, 2024, **67**, 2583–2589.

187 Y. Zhang, M. Chen, X. Wang, M. Lin, H. Wang, W. Li, F. Chen, Q. Liao, H. Chen, Q. Chen, M. Lin and H. Yang, Efficient and Fast X-Ray Luminescence in Organic Phosphors Through High-Level Triplet-Singlet Reverse Intersystem Crossing, *CCS Chem.*, 2024, **6**, 334–341.

188 X. Du, S. Zhao, L. Wang, H. Wu, F. Ye, K.-H. Xue, S. Peng, J. Xia, Z. Sang, D. Zhang, Z. Xiong, Z. Zheng, L. Xu, G. Niu and J. Tang, Efficient and ultrafast organic scintillators by hot exciton manipulation, *Nat. Photonics*, 2024, **18**, 162–169.

189 T. J. Hajagos, C. Liu, N. J. Cherepy and Q. Pei, High-Z Sensitized Plastic Scintillators: A Review, *Adv. Mater.*, 2018, **30**, 1706956.

190 J. Hui, P. Ran, Y. Su, L. Yang, X. Xu, T. Liu and Y. M. Yang, High-Resolution X-ray Imaging Based on Solution-Phase-Synthesized Cs3Cu2I5 Scintillator Nanowire Array, *J. Phys. Chem. C*, 2022, **126**, 12882–12888.

191 Z. Zhang, H. Dierks, N. Lamers, C. Sun, K. Nováková, C. Hetherington, I. G. Scheblykin and J. Wallentin, Single-Crystalline Perovskite Nanowire Arrays for Stable X-ray Scintillators with Micrometer Spatial Resolution, *ACS Appl. Nano Mater.*, 2021, **5**, 881–889.

192 J. Hui, P. Ran, Y. Su, L. Yang, X. Xu, T. Liu, Y. Gu, X. She and Y. Yang, Stacked Scintillators Based Multispectral X-Ray Imaging Featuring Quantum-Cutting Perovskite Scintillators With 570 nm Absorption-Emission Shift, *Adv. Mater.*, 2025, **37**, 2416360.

193 Z. Lin, S. Lv, Z. Yang, J. Qiu and S. Zhou, Structured Scintillators for Efficient Radiation Detection, *Adv. Sci.*, 2021, **9**, 2102439.

194 C. Roques-Carmes, N. Rivera, A. Ghorashi, S. E. Kooi, Y. Yang, Z. Lin, J. Beroz, A. Massuda, J. Sloan, N. Romeo, Y. Yu, J. D. Joannopoulos, I. Kaminer, S. G. Johnson and M. Soljačić, A framework for scintillation in nanophotonics, *Science*, 2022, **375**, eabm9293.

195 X. Xu, Y. M. Xie, H. Shi, Y. Wang, X. Zhu, B. X. Li, S. Liu, B. Chen and Q. Zhao, Light Management of Metal Halide Scintillators for High–Resolution X–Ray Imaging, *Adv. Mater.*, 2024, **36**, 2303738.

196 H. Dierks, Z. Zhang, N. Lamers and J. Wallentin, 3D X-ray microscopy with a $CsPbBr_3$ nanowire scintillator, *Nano Res.*, 2022, **16**, 1084–1089.

197 L. Yi, B. Hou, H. Zhao, H. Q. Tan and X. Liu, A double-tapered fibre array for pixel-dense gamma-ray imaging, *Nat. Photonics*, 2023, **17**, 494–500.

198 W. Shao, T. He, L. Wang, J. X. Wang, Y. Zhou, B. Shao, E. Ugur, W. Wu, Z. Zhang, H. Liang, S. De Wolf, O. M. Bakr and O. F. Mohammed, Capillary Manganese Halide Needle–Like Array Scintillator with Isolated Light Crosstalk for Micro–X–Ray Imaging, *Adv. Mater.*, 2024, **36**, 2312053.

199 J. Song, Y. He, H. Hu, M. Li, C. Li, B. Yang and H. Wei, Anti-Scattering Perovskite Scintillator Arrays for High-Resolution Computed Tomography Imaging, *Adv. Mater.*, 2025, **37**, 2417248.

200 W. Shao, T. He, J.-X. Wang, Y. Zhou, P. Yuan, W. Wu, Z. Zhang, O. M. Bakr, H. Liang and O. F. Mohammed, Transparent Organic and Metal Halide Tandem Scintillators for High-Resolution Dual-Energy X-ray Imaging, *ACS Energy Lett.*, 2023, **8**, 2505–2512.

201 X. Hu, S. Luo, J. Leng, C. Wang, Y. Chen, J. Chen, X. Li and H. Zeng, Density-discriminating chromatic X-ray imaging based on metal halide nanocrystal scintillators, *Sci. Adv.*, 2023, **9**, eadh5081.

